Journal of Materials Chemistry A

Applications of MAX phases and MXenes as catalysts

Journal:	*Journal of Materials Chemistry A*
Manuscript ID	TA-REV-05-2021-004097.R1
Article Type:	Review Article
Date Submitted by the Author:	14-Jul-2021
Complete List of Authors:	Chirica, Maria-Iuliana; National Institute of Materials Physics; University of Bucharest, Faculty of Physics Mirea, Anca ; National Institute of Materials Physics Neatu, Stefan; National Institute of Materials Physics Florea, Mihaela; National Institute of Materials Physics Barsoum, Michel; Drexel University, Department of Materials Science and Engineering Neatu, Florentina; National Institute of Materials Physics, 405 A, Atomistilor Street, 077125, Bucharest, Romania

SCHOLARONE™
Manuscripts

REVIEW

Applications of MAX phases and MXenes as catalysts

Iuliana M. Chirica,[a,b] Anca G. Mirea,[a] Ștefan Neațu,[a] Mihaela Florea,*[a] Michel W. Barsoum,*[c] and Florentina Neațu*[a]

Received 00th January 20xx,
Accepted 00th January 20xx

DOI: 10.1039/x0xx00000x

MAX phases and MXenes are important materials that have recently gained great popularity due to their special properties, which renders particularly useful in many applications, including catalytic ones. This can be seen in the large number of publications that appear annually on these materials and their applications. This review aims to evaluate the MAX phases and MXenes as materials in heterogeneous, non-electrocatalytic, catalytic applications. The review begins with a brief introduction to the MAX phase and MXene properties that recommend them as potential materials for heterogeneous catalytic applications, followed by four sections grouped according to the processes in which they have already proven effective. These include supports to activate the C–H or C–O bonds in applications such as dehydrogenation of light or aromatic alkanes, methanol formation from CH_4, dry reforming, CO oxidation or water gas shift reaction (Section 2), their use in fine chemical reactions (Section 3) and in chemical degradation (Section 4). The last section deals with photocatalytic applications (Section 5). The review ends by highlighting huge potential of these materials for a wide range of heterogeneous catalytic applications as well as the challenges ahead.

1. Introduction

The MAX phases ($M_{n+1}AX_n$) and their derivatives, MXenes ($M_{n+1}X_nT_x$), (with n = 1–4, M = early transition metal, A = A-group element, X = carbon or nitrogen and T_x = various surface terminations, such as –O, –OH and –F) are a relatively new class of materials that have been discovered in the last two decades.[1–3] They have impressed by the multitude of physical and chemical properties they are endowed. These materials manage to bring together two completely different classes of materials (ceramics and metals) by weaving important properties from both classes, like high thermal and electrical conductivity, mechanical strength and low density. Moreover, MAX phases possess also resistance to high temperatures or oxidation.

Presently, over 150 MAX phases[4], and more than 30 MXenes with different compositions have been synthesized.[5] The unique MAX phases properties arise from their lamellar structure, metallic/covalent bonds, together with relatively weak bonds between the M and A layers.

The presence of oxygenated terminations, preserves the high conductivity even in polar media.[2] Thus, as a result of all these interesting properties MAX phase and MXene are highly desirable and attractive materials for catalysis, but despite all evidences that recommend them as catalysts, their catalytic properties were investigated only recently[6] and fortunately the interest is increasing exponentially (see Fig. 1) and is expected to grow considerably in the future.

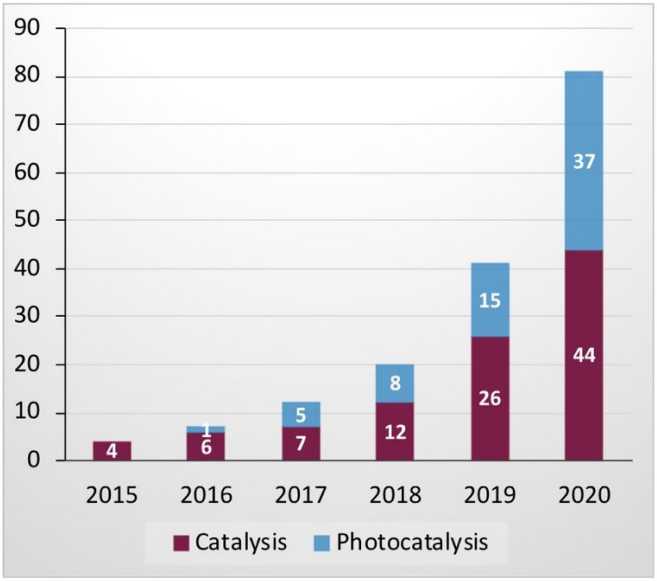

Fig. 1 MAX phase and MXene publications in catalysis and photocatalysis fields (data collected from www.webofknowledge.com (May 2021, electrocatalysis was excluded).

[a] National Institute of Materials Physics, 405A Atomistilor street, 077125 Magurele, Romania; E-mails: mihaela.florea@infim.ro and florentina.neatu@infim.ro
[b] University of Bucharest, Faculty of Physics, 405 Atomistilor street, 077125 Magurele, Romania;
[c] Department of Materials Science & Engineering, Drexel University, Philadelphia, PA 19104, USA; E-mail: barsoumw@drexel.edu

† Footnotes relating to the title and/or authors should appear here.
Electronic Supplementary Information (ESI) available: [details of any supplementary information available should be included here]. See DOI: 10.1039/x0xx00000x

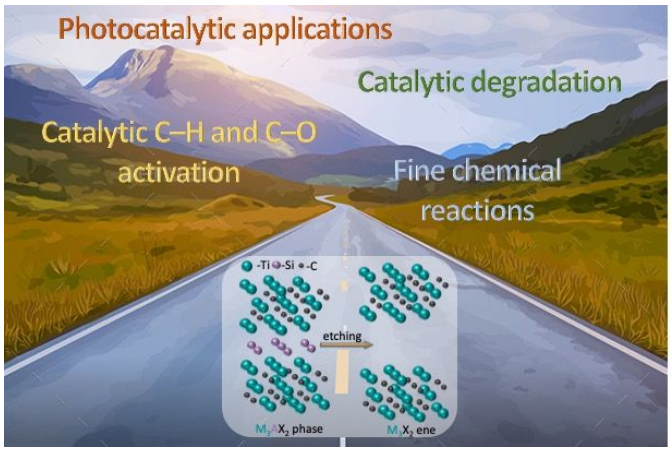

Scheme 1. Applications road map for the MAX phases and their MXene derivatives.

Up to now, there are several excellent reviews about MXene and MXene-based materials that focus on the preparation, property, and potential applications.[1–3,5,7–10] However, a comprehensive and systematic review on recent progress of the use of the MAX phases and MXene-based materials in catalytic applications is lacking. In this review, we intend to present general aspects to be considered, and to outline which are currently the most efficient catalytic systems based on these materials in: i) catalytic processes centred on C–H and C–O activation, ii) fine chemical reactions, iii) catalytic degradation, and iv) photocatalytic applications. An applications roadmap is depicted in Scheme 1. Note that there are already several review papers that cover photocatalytic materials up to 2020.[11–14] Here we thus only focus on the last two years (2020 or 2021). Moreover, in this review we are not discussing MAX phase and MXene materials as catalysts for electrochemical applications. Readers can refer to other comprehensive reviews in that area.[15–17]

2. Processes based on C–H and C–O activation (theoretical and experimental studies)

The mind map illustrated in Scheme 2 summarize the materials use in C–H and C–O bonds activation and their corresponding catalytic reactions.

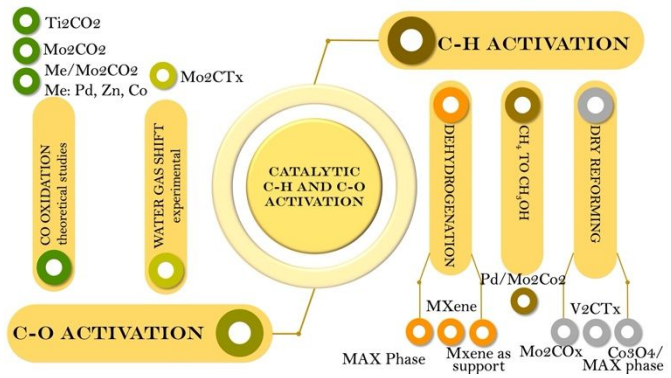

Scheme 2. Types of MAX phases and MXene used in processes based on C–H and C–O activation.

2.1. C–H activation

Dehydrogenation reactions. As noted above, the physical, electrical and optical properties of the MAX phases and their MXenes in general have been intensively studied recently. Much less work, however, has been devoted to their catalytic properties.

Direct dehydrogenation (DDH) and oxidative dehydrogenation (ODH) of hydrocarbons are important reactions for obtaining alkenes monomers, that are, in turn, key intermediates in the polymer industry. Some of the important monomers include n-butene or 1,3-butadiene starting from n-butane[18] or styrene synthesized from ethylbenzene[19].

Usually these processes require high temperatures (~600 °C) and excess steam and suffer of catalyst deactivation due to the formation of coke. The MAX phases and MXenes show activity and long-term stability in these types of reactions.

MAX phase as catalysts. Ti_3AlC_2 is one of the first MAX phases, which was reported to be a good catalyst in n-butane ODH reaction with long-term stability.[6]

Oxidative reactions in general, and ODH in particular, are recognised to take place through redox mechanisms, meaning that the catalyst in a higher oxidation state oxidizes the reactants, while it is being reduced, and the oxygen re-oxidizes the catalyst surface to restart a new cycle.[20,21] This mechanism - also known as Mars-Van-Krevelen mechanism - is associated with oxide materials and usually metallic oxides or metals supported on metallic oxides.[22]

The most intriguing part is that the MAX phase, albeit presents combined metallic and ceramic properties do not present an oxygen lattice, which apparently is a prerequired for oxidative reactions. However, Ti_3AlC_2 not only is active (24% conversion) in n-butane ODH, but it is also quite selective (a total selectivity of 50% in butenes and butadiene), which is a remarkable result.[6] It is difficult to achieve simultaneously active and selective catalysis, because conventional conditions to activate n-butane are too harsh and typically lead to total oxidation of n-butane (CO_2 and H_2O). The authors supposed that in absence of oxygen lattice, the adsorption of oxygen highly depends on the defects content of the surface oxide, which can also act as active sites. HRTEM data showed the presence of a large number of defects (points, domains or layers defects), while Positron Annihilation Lifetime Spectroscopic analyses confirmed the presence of Ti monovacancy defects and vacancy clusters and voids. The presence of a thin oxide layer at the surface (Al–Ti–O), with a high oxygen content (HRTEM, XPS, EDX mapping) that is believed to have a synergy with the electron reservoir below it, is believed to be responsible for the Ti_3AlC_2 activity in n-butane ODH. To confirm this assumption, computational evaluation for the possible mechanisms was considered, starting from the presumption that stable ternary phase of Al_2TiO_5 is present on the surface and it is oxygen terminated. Firstly, the DFT calculations showed that butane adsorbs relatively easily, through the formation of a C–O bond on the selected surface. Also, the DFT calculations indicated that oxidative dehydrogenation of *n*-butane is energetically favourable on the MAX phase surface and moreover, the

This journal is © The Royal Society of Chemistry 20xx

Please do not adjust margins

presence of defects and the existence of a superficial non-stoichiometric oxide surface layers rich in oxygen vacancies promote this material as a potential catalyst, able to transform *n*-butane in butene or/and butadiene.

MXene as catalysts. Due to the similarities found between graphenes and MXenes ($Ti_3C_2T_x$), the abundance of the functionalities on the surface (T_x) and the versatile properties of the latter, Diao *et al.*[23] investigated this class of materials in ethylbenzene DDH. Until this report, C-based materials have improved the overall process of ethylbenzene DDH and is believed that active sites in DDH reaction on 2D materials (e.g., graphenes), is due to the flat surface and an enriched oxygenated functionality (e.g., C=O) at the catalysts interface.[24,25]

The results obtained by Diao *et al.*[23] showed that $Ti_3C_2T_x$ was not only suitable for this catalytic reaction, but increased ethylbenzene's DDH activity to 92 µmol m^{-2} h^{-1}, ~8 times higher than that of graphene. Combining experimental and theoretical first-principles calculations it was concluded that the surface C–Ti–O groups and the layered structure of MXene, that facilitate the mass transfer and adsorption–desorption processes, are responsible for the catalytic performance of Ti_3C_2Tx in ethylbenzene dehydrogenation reaction. Noteworthily, the selectivity of ethylbenzene DDH on Ti_3C_2Tx was 97.5%, indicating very few side products. Thus, experimentally, the layered structure of MXenes has been demonstrated to bring an important value to the DDH reaction. Interestingly, the MAX phase precursor - Ti_3AlC_2 - reactivity was close to zero.

Figure 2 presents the mechanism details of ethylbenzene dehydrogenation on $Ti_3C_2T_x$. The functional groups, T_x, found onto the surface were C–Ti–O (high percentage), C–Ti–OH and C–Ti–F. At higher temperatures, the last two functionalities are prone to transform to C–Ti–O groups, that are believed to be responsible for the impressive activity of $Ti_3C_2T_x$. Additionally, $Ti_3C_2T_x$ has the advantage to remain active for a long time (40 h) without any deactivation. Transmission electron microscope, TEM, images evidenced the absence of coke onto the surface, underscoring the stability of this material for ethylbenzene DDH. Besides the experimental evidence, the authors performed theoretical calculations to highlight both, the MXene properties and the active sites responsible for this improved activity.[23]

Computational studies also, demonstrated that C–Ti–O can perform the ethylbenzene dehydrogenation by approaching the ethylbenzene in a parallel way and activating the C–H bond (0.66 eV) with the O found on the surface. The second dehydrogenation is possible due to the abundance of the O on the MXene surface and diffusion of the hydrogen to a neighbouring O (Fig. 2).

MXenes as catalytic support. The presence of noble metals as nanoparticles onto a support such as MXenes can favor the reduction of metal (M) from MXene and/or the removal of surface functional groups.[26]

Such interaction drives the formation of bimetallic structures that form ordered intermetallic compounds (IMC) that are quite thermodynamically stable. This type of interaction can occur at lower temperatures facilitating the control of the noble metal particles size. For example, Li *et al.*[27] formed Pt_3Ti and Pt_3Nb IMCs with Cu_3Au type structure when Pt was supported on $Ti_3C_2T_x$ and Nb_2CT_x MXenes, respectively. These compounds are extremely active in light alkanes dehydrogenation. The reactivity is due to the Pt-M ordered intermetallic structures, which was evidenced by high resolution TEM microscopy (see Fig. 3), EXAFS an XANES.

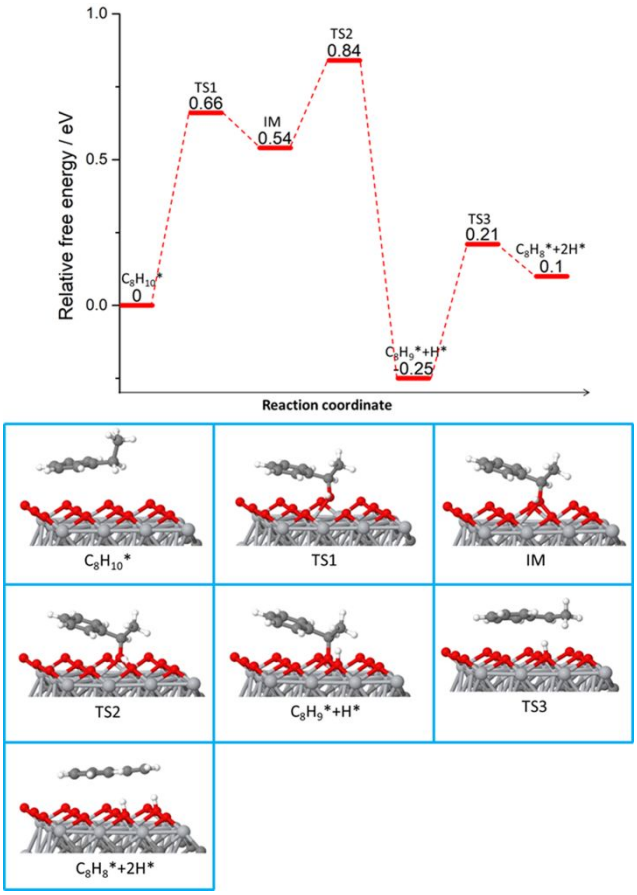

Fig. 2 Reaction pathway and important structures of ethylbenzene dehydrogenation on $Ti_3C_2O_2$. Ti is shown in light gray, C in dark gray, O in red, and H in white. Reprinted with permission from Ref. [23], Copyright 2018 American Chemical Society.

These materials were tested in propane and isobutane dehydrogenation. In term of activity, $Pt/Ti_3C_2T_x$ and Pt/Nb_2CT_x were comparable with Pt/SiO_2 (15%), but result in higher selectivity (90-95%) than standard catalysts (60%) in propylene formation. The influence of particle size over selectivity (smaller particles, higher selectivity) was excluded, because the intermetallic compounds presence was larger than those on Pt/SiO_2. The increase in selectivity was related to the formation of IMCs. Contrary to classical catalysts, these materials, as explained by density functional theory, DFT, preserve the selectivity even at high values of activity and are stable under long-term reaction conditions. DFT showed that in the first steps of the reaction, Pt (111) found in Pt/SiO_2 is more energetically privileged to adsorb and activate C–H bond than Pt_3Ti (111), but in the following steps, the formation of

secondary products is not favoured on Pt_3Ti (111). The experimental results and DFT calculations show that this is due to the lower barrier desorption of olefins compared with the deep dehydrogenation energy calculated on Pt_3Ti (111), in opposite to the behaviour observed for the Pt (111), thus explaining the high selectivity of Pt/MXene catalysts.

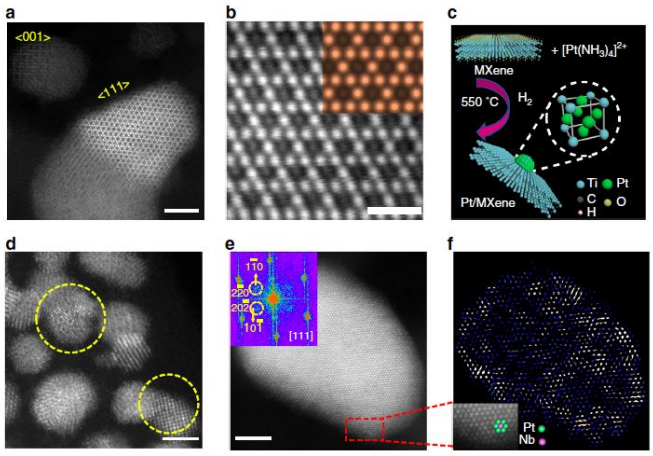

Fig. 3 TEM characterizations of 1 wt.% Pt/MXene catalysts. **a** Representative HAADF-STEM image of 1% $Pt/Ti_3C_2T_x$ catalyst. **b** (111) surface of Pt_3Ti NP. Inset is a simulated STEM image of Pt_3Ti (111) surface. Simulated image is in good agreement with the experimental results. **c** Schematic illustration of reactive metal-support interactions in Pt/MXene catalysts and the structure of L12-ordered intermetallic Pt_3Ti. **d** Representative HAADF STEM image of 1% Pt/Nb_2CTx catalyst. **e** Pt-Nb NP viewed along [111], inset is the FFT pattern of the NP. **f** IFFT pattern of the NP in Fig. 3e. Inset is enlarged image showing the superlattice of the NP. Scale bars: **a**, **d**, **e** 2 nm, and **b** 500 pm. Reprinted from Ref. [27] (open access).

CH_4 to methanol. Besides the formation of ordered IMCs on MXenes, other theoretical studies have shown that supporting different noble metals on MXenes can facilitate the formation of single-atom catalysts (SACs). Surface defects from the supports have been found to play a crucial role in stabilizing single atoms.[28] It follows that MXenes, due to their 2D structure and defective surfaces, allow SACs formation and enhance the stability of SACs without affecting their activity or selectivity. For instance, by using DFT calculations Wang *et al.*[29] demonstrated that single atoms of Pd monomer, and dimers anchored on Mo_2CO_2, where the oxygen in the formula indicates that the 2D system is O-terminated, can be stable and active for C–H bond activation. Moreover, theory showed that Mo_2CO_2 could be an ideal support to anchor Pd dimer and can be considered a high-activity catalyst with sufficient structural stability for the direct conversion of methane to methanol. CH_4 and O_2 can stably adsorb on the Pd-dimer/Mo_2CO_2 surfaces due to the existence of multiple adsorption sites.

Dry reforming. In 2020, the same material, Mo_2CO_2 was dispersed on silica and found to provide high stability and catalytic activity in the dry reforming of methane, CH_4 (DRM)[30] (see equation 1).

$$CH_4 + CO_2 \rightarrow 2CO + 2H_2, \quad \Delta H^0_{298K} = 247 \text{ kJ mol}^{-1} \qquad (1)$$

Theoretical and experimental results indicated that CH_4 activation is the rate-limiting step in agreement with the results of Wang *et al.*[29] The characterization data, such as XANES and XPS analysis suggested that the 2D Mo_2CO_x contains Mo, with an average oxidation state of +4, that is the active phase for dry reforming of CH_4. This was also supported by DFT calculations, which showed that CH_4 activation on oxygen sites to form $*OCH_3$ and *OH is endergonic by 105 kJ mol^{-1}, which is 45 kJ mol^{-1} less favourable than CH_4 activation on the Mo sites of the same surface. Another key step in the dry reforming of CH_4 is the oxidation of either CH* or C* species on the oxycarbide surface by adsorbed oxygen (O* or structural oxygen)[31] to produce CO*. In the case of 2D-Mo_2CO_x, and in contrast to metallic surfaces[32], DFT calculations showed that the preferred mechanism is the direct oxidation of adsorbed C* by adsorbed O* to form CO*.

The idea of depositing MXene on silica was to prevent the thermal transformation to bulk Mo_2C and MoO_2 phases, in this way opening new avenues for the application of 2D Mo-carbides and oxycarbides for high temperature heterogeneous catalysis. Indeed, the nanosheet morphology of 2D-Mo_2CO_x was maintained during catalysis and regeneration processes. Moreover, the 2D nature provides a very high utilization of Mo. For instance, when normalized by weight of Mo, the initial CH_4 consumption rate of 2D-Mo_2CO_x/SiO_2 was ~10–200 times higher than the rates that have been reported for other Mo_2C based catalysts under similar reaction conditions.

This was not the case when multilayer V_2CT_x MXene (m-V_2CT_x) was used as catalyst in the DRM. Carrero *et al.* revealed that V_2CT_x MXene transforms during reaction into an oxycarbide with the following composition: V_2O_3–V_8C_7/m-V_2CT_x after exposure to CH_4 and CO_2.[33] This oxy-carbide phase shows interesting activity for DRM, converting about 78% CH_4 and 82% of CO_2 with CH_4 and CO_2 conversion rates of 153.4 $mmol_{CH4}mol_V^{-1}$ min^{-1} and 178.2 $mmol_{CO2}mol_V^{-1}$ min^{-1}, respectively. The authors concluded that, these results are comparable to Ni-based catalysts[34] and are about four times higher than the parent bulk V_2AlC MAX phase or VC.

The same V-based MXene was also reported as a good catalysts for dehydroaromatization of CH_4.[35] The multi-layered, ML, 2D V_2CT_x transformed CH_4 in benzene at 700 °C, with similar results as the benchmark Mo/ZSM-5 catalyst (11.8% activity, 4.84% yield at a rate formation of 1.9 mmol $g_{cat}^{-1}h^{-1}$). Besides the great importance of CH_4 dehydroaromatization (MDA) to produce liquid aromatics, this reaction is also extremely important from a fundamental point of view, to establish the reaction mechanism for C-H activation. Correlation of experimental data and operational Raman spectroscopy evidenced the presence of 2D-VC and 2D-V=O, and the formation of C_2H_2, H_2, and benzene. The authors propose the V–C bond as an active site for C–H activation, followed by the formation of dimers, between the V_2CT_x layers (~7.0 Å) (see Fig. 4). Oligomers and benzene formation requires acidic sites, which are associated with the presence of terminal functional groups (e.g., OH and O-) and/or are due to the presence of unreacted V_2AlC MAX phase. Further studies are needed to conclusively better understand this reaction.

This journal is © The Royal Society of Chemistry 20xx

Please do not adjust margins

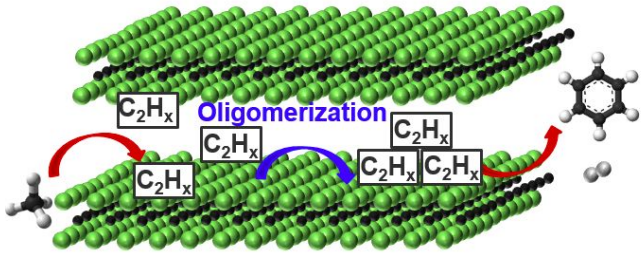

Fig. 4 MDA reaction scheme over *m*-V_2CT_x MXene forming C_6H_6 and H_2 as the main reaction products. Reprinted with permission from Ref. [35], Copyright 2020 Wiley Online Library.

This material attracted interest, due to the fact that is stable at high temperatures[36]. Unfortunately, like in the benchmark catalyst, deactivation due to the deposition of graphitized C occurs. The deactivation rate for MXene, however, is lower. Comparing the catalytic activity in DRM for the two MXenes, Mo_2CTx and V_2CT_x, was observed that Mo_2CTx is not active at all, while V_2CT_x is active but only after the in-situ transformation into an oxycarbide with the following composition V_2O_3–V_8C_7/m-V_2CT_x. By supporting Mo_2CTx on silica and after CO_2 treatment a composite, Mo_2CO_x/SiO_2, that is as active as V_2O_3–V_8C_7/m-V_2CT_x was obtained.

Based on the results obtained on direct dehydrogenation of *n*-butane, Ronda-Lloret *et al.*[37] surface modified Ti_2AlC with Co_3O_4, to allow butane dry reforming. For butane dry reforming the acidity of the material and also the good dispersion of the active sites are important considerations. Ti_2AlC has 10 times lower acidity than Al_2O_3 and its use as support should release a catalyst which deactivates slower than the benchmark catalysts (Co_3O_4/Al_2O_3 and Co_3O_4/TiO_2). Indeed, Co_3O_4/Ti_2AlC has a lower activity (35%) than the Co_3O_4/Al_2O_3 (60%) catalysts, but a much higher selectivity to CO and H_2. The use of Ti_2AlC as support generates special agglomeration of Co_3O_4 particles in form of hollow spheres, 90-500 nm in diameter, with small voids (6-30 nm), that are unlike the Co_3O_4 particles supported onto alumina or titania. The appearance of hollow spheres and small voids is associated to the special features of MAX phase containing Ti–C and Ti–Al bonds, which allows the Kirkendall effect (different diffusion rates of the cations and anions during oxidation) to take place on the surface. Contrary to TiC, which decomposes to graphite and TiO_2, Ti_2AlC is quite stable under dry reforming conditions. With time, the Co_3O_4/Ti_2AlC surface becomes covered by carbon nanotubes, but the rate of coke deposition is much lower than that of the benchmark catalysts.

2.2. C–O activation

CO oxidation. Zhou *et al.*[38] carried out a theoretical study in which they studied CO oxidation on single Ti atoms anchored on a typical MXene monolayer, Ti_2CO_2. The main idea was to employ Ti_2CO_2 monolayers in order to prevent the formation of Ti clusters, and therefore to increase the intrinsic activity, efficiency and stability of the catalyst. From Fig. 5, which depicts the optimized energetically most favourable structures of O_2 and CO adsorbed on Ti-anchored on $TiCO_2$, it is obvious that the catalyst could efficiently capture the reactants (O_2 and CO), and the adsorption energy of O_2 is higher than that of CO.

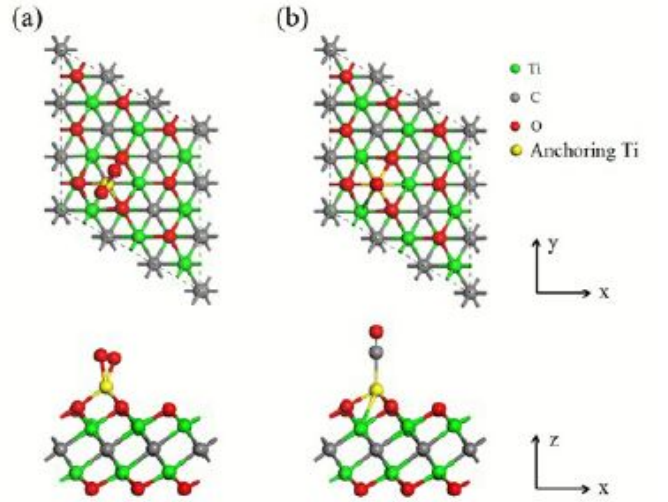

Fig. 5 Energetically most favorable structures of, a) O_2 and b) CO adsorbed on Ti-anchored Ti_2CO_2 (top upper) and side (lower) views). Reprinted with permission from Ref. [38], Copyright 2016 Royal Society of Chemistry.

Data obtained using first-principles computations indicated that the Eley-Rideal mechanism may be preferred under specific experimental conditions. Moreover, due to the fact that, the energy barriers are comparable to many noble metal catalysts the results demonstrated that Ti/Ti_2CO_2 do not need a noble metal to exhibit high activities for CO oxidation.

Another theoretical study of CO oxidation was reported using MXene as support for single Pd atom anchored on Mo_2CO_2 monolayers.[39] The key point of this study was the comparison of pristine and defective Mo_2CO_2 monolayers with an oxygen vacancy (denoted as O_V-Mo_2CO_2). In the same line with previous results,[38] Pd/O_V-Mo_2CO_2 was found to be highly active in CO oxidation and can achieve comparable catalytic activity to those containing noble metals. Moreover, the authors found that Pd/O_V-Mo_2CO_2, due to the fact that single Pd atom can modify the electronic structure, has higher catalytic activity than iron embedded graphene,[40] copper embedded graphene,[41] Pd-anchored graphene oxide and Pd-embedded vacancy graphene[42] or Pd@TiO_2(110)[43] studied in the same reaction. Contrary to the results obtained on Ti anchored on Mo_2CO_2[38] for which the Eley-Rideal mechanism is preferred, on Pd supported on Mo_2CO_2 among the three mechanisms studied, Eley-Rideal, Langmuir-Hinshelwood and termolecular Eley-Rideal, the latter is more preferable because of a small reaction barrier (0.49 eV) and can occur at lower temperatures. Moreover, the adsorbed CO molecules themselves could promote O_2 activation to easily form CO_2, due to the fact that that CO could transfer electrons to the O_2-2π* orbitals and induce O–O bond scission, in a process similar to the one found in gold cluster catalysts. It is demonstrated that defective MXenes may be used as supports for stable SACs, in agreement with other reported results.[38]

Indeed, in 2019, also on the basis of first-principles calculations, different metals (M), such as Fe, Co, Ni, Cu, Zn, Ru,

Rh, Ag, Ir, Pt, and Au were decorated on defective $Mo_2CO_{2-\delta}$ monolayers and investigated as SAC candidates for low-temperature CO oxidation reaction.[44] This study showed that the binding energies (E_{bind}) variations as the M atomic number increased (see Fig. 6) are similar for the three transition metal periods, but that the M-surface binding become much weaker toward the end of the period, due to the fact that Cu, Zn, Ag, and Au have fully occupied d orbitals, so less free orbitals available to participate in bonding with the MXene atoms.

From the calculated data it seems that $Zn/Mo_2CO_{2-\delta}$ has the weakest binding strength because of the fully filled 3d and 4s orbitals. Also, Zn is the only M that has a negative E_{diff} value (E_{diff} is the difference between binding energy and cohesive energy), while the other metals (Fe, Co, Ni, Cu, Ru, Rh, Ir, and Pt) have positive E_{diff} values, indicating a strong tendency for clustering and they are, at least in this respect, not promising SAC candidates.

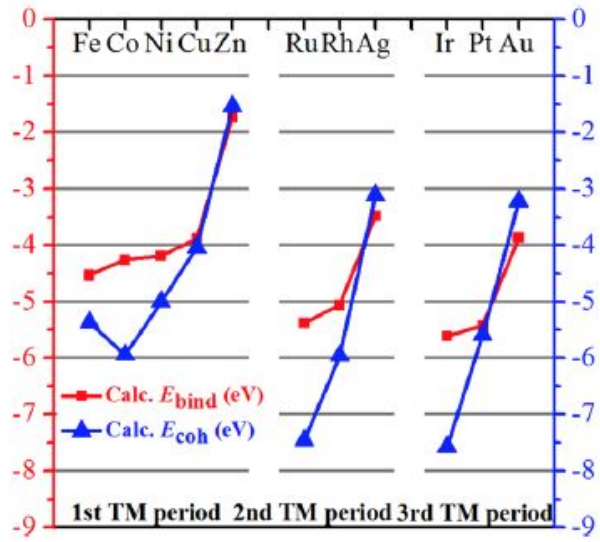

Fig. 6 Calculated binding energy (E_{bind}, red squares, left y-axis) and the corresponding bulk cohesive energy (E_{coh}, blue triangles, right y-axis) for $M/Mo_2CO_{2-\delta}$ (M = Fe, Co,Ni, Cu, Zn, Ru, Rh, Ag, Ir, Pt, and Au). Reprinted with permission from Ref. [44], Copyright 2019 John Wiley and Sons

Therefore, based on well-established intuitive criteria concerning metal sintering, CO poisoning, and O_2 adsorption strength, $Zn/Mo_2CO_{2-\delta}$ system was selected for reactivity calculations as a function of CO concentrations. The authors suggested that at low CO concentrations, the oxidation reaction will predominantly proceed via the Eley-Rideal mechanism as it has a small energy barrier of 0.15 eV. In this case also, the main conclusion was that $Zn/Mo_2CO_{2-\delta}$ represent a potential candidate for low-temperature SAC applications that have a lower energy barrier for CO oxidation than noble metals and other 2D SAC systems.[44]

Along the same lines, to design stable SACs, a systematic screening was performed using first principles calculations based on the density functional theory.[45] More precisely, this study concerns different metal atoms such as Sc, Ti, V, Cr, Mn, Fe, Co, Ni, Cu, Zn, that are deposited on different MXene surfaces with M_2C stoichiometry (M = Ti, V, Cr, Zr, Nb, Mo, Hf, Ta, and W).[45] As in previous case,[44] Zn atoms attached on MXene surfaces appear as the most stable SAC due to the fact that surface diffusion is hindered by moderate energy barriers. The calculations data also showed that all 3d metal studied atoms interact exothermically with MXene substrates and that the properties of the SAC can be tuned by suitably matching the two components of the resulting M@MXene. The results obtained are in good agreement with analogous SAC studies on graphene[46] and graphynes.[47]

Last year, using the same approach, Co deposited on Mo_2CO_2 has been used to investigate the CO oxidation by O_2.[48] In agreement with previous results it was shown that Co strongly bonds to a defective Mo_2CO_2 surface, and that CO adsorption is more favourable than O_2 adsorption. The relatively small activation energy barriers indicate that Eley-Rideal, Langmuir-Hinshelwood and termolecular Eley-Rideal mechanisms are all possible at low temperatures.

Unfortunately, no experimental studies on CO oxidation reaction using MXene as support was found in the literature, but we hope that the theoretical data presented in this review will pave the way for experimentalists to develop practical experiments in the near future. We emphasize here that before starting such experiments, the oxygen partial pressure in the system must be estimated and compared to that of the oxidation of the metal used. If the partial pressure is higher they will oxidize, which may or may not be useful.

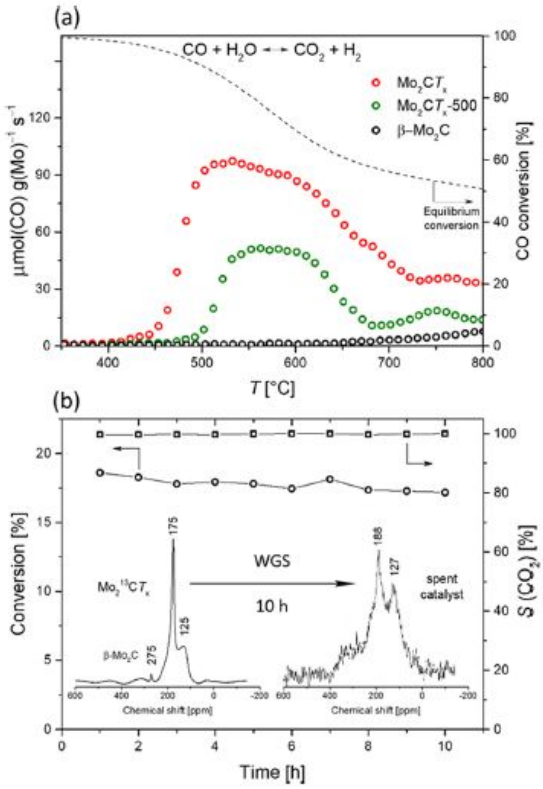

Fig. 7 (a) WGS catalytic activity of Mo_2CT_x, Mo_2CT_x-500, and β-Mo_2C and (b) WGS stability test of Mo_2CT_x at 500 °C and ^{13}C MAS NMR (400 MHz, spinning rate 10 kHz) of $Mo_2{}^{13}CT_x$ before (1200 scans) and after (20 000 scans) WGS catalytic test. Reprinted with permission from Ref. [49] Copyright 2019 American Chemical Society

This journal is © The Royal Society of Chemistry 20xx

Please do not adjust margins

The first experimental example involving CO activation on MXene is the water gas shift, WGS, reaction. In 2019, Deeva *et al.* demonstrated the stability of layered MXene structures based on Mo, in reducing environments when heated up to 550-600 °C. At higher temperatures (>730 °C), a bulk β-Mo_2C was evidenced.[49] To probe the catalytic properties, Mo_2CT_x was tested in the WGS reaction. In Fig. 7 its catalytic activity is compared with samples treated at 500 °C and a reference β-Mo_2C. As expected, due to the surface functional groups, Mo_2CT_x showed a higher activity than the other catalysts. The highest activity was recorded at 520 °C with a peak consumption rate of CO at ca. 100 μmol (CO) $g(Mo)^{-1}$ s^{-1}. Interestingly, this value is comparable to weight normalized rates of CO consumption obtained on conventional Fe-based WGS catalyst, i.e., Fe/Ce/Co oxide,[50] as well as by a 3.9 wt % Pt/Al_2O_3 catalyst[51]. At temperatures > 700 °C, the activity of Mo_2CT_x diminished, however, the conversion values were still higher than other tested samples. It is important to note here that this Mo_2CT_x catalyst showed high stability in O-rich environments at high temperatures, as depicted in Fig. 7b and confirmed by XRD analysis, which shows that the tested Mo_2CT_x contained only trace amounts of MoO_2.

These results, represent the first proof demonstrating that Mo_2CT_x is a robust catalyst for high-temperature catalytic applications and that it is particularly stable against oxidation to MoO_2.

3. Fine chemical reactions

Fine chemical reactions are an important class of chemical transformations, in which MXenes are starting to be explored[52–55] as catalysts due to their interesting properties (Scheme 3).

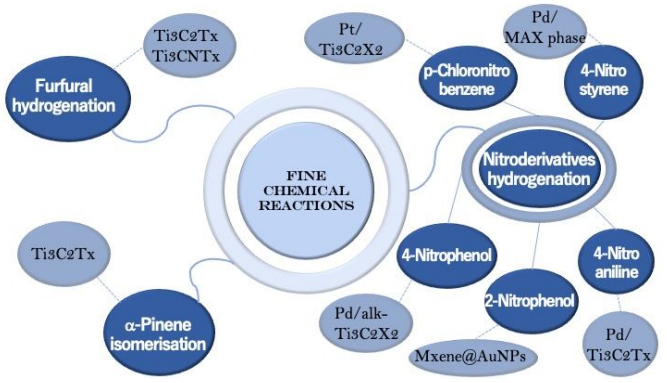

Scheme 3. Types of MAX phase and MXene used in fine chemical reactions.

Isomerization of α-pinene. Recently, Zielińska *et al.*[56] tested $Ti_3C_2T_x$ as a catalyst for the α-pinene isomerization reaction to camphene, one of the most pervasive monoterpenes. The target point of this catalytic process is to produce camphene with high selectivity because it is of great importance in the perfumery industry,[57] as an intermediate in organic synthesis. Lately, there have also been studies[58] confirming its anticancer properties.

The catalytic activity of Ti_3C_2 and exfoliated-Ti_3C_2 (ex-Ti_3C_2) was studied in α-pinene isomerisation and was found that ex-Ti_3C_2 displays higher activity (60% conversion) than the unmodified Ti_3C_2 catalyst (48% conversion) and similar selectivity for camphene (~59 mol.%).[56] There are many key factors that can explain the superior catalytic activity of ex-Ti_3C_2, particularly the higher specific surface area and the higher amount of acid sites of this catalyst.

Briefly, it was shown that ex-Ti_3C_2 shows much higher activity (100 mol% conversion of α-pinene in 7 h of process) compared with the multilayered Ti_3C_2. Moreover, the catalytic reactions were performed with smaller amount of catalyst and without solvent. The kinetics modelling was studied and the proposed pattern was well fitted to the experimental data for the isomerization of α-pinene; the reactions over both catalysts followed first-order kinetics. Additionally, the selectivity of the product of interest at 100% conversion is ~2 times higher for Ti_3C_2 MXenes compared with others Ti-based catalysts such as Ti-SBA-15 and Ti-MCM-41. Moreover, undesired dimerization and polymerization reactions were not detected.[56]

Hydrogenation of nitroderivates. Catalytic hydrogenation reactions are among the most important reactions concerning the industrial production of chemicals.[59,60]

Selective hydrogenation is difficult, [61] especially when it is possible to hydrogenate more than one functional group per molecule of reactant.[62] Heterogeneous metal-based catalysts possess chameleonic properties and are good materials to be developed for selective catalytic hydrogenation toward desired reaction products.[63] So, in the case of nitroderivates, the selective reduction of the $–NO_2$ groups while preserving intact the other reducible groups is highly desirable, but not easy. Typically, the nitrostyrene molecule, usually used as substrate, is considered to be the most demanding because the –C=C bond is quite sensitive and, consequently, more susceptible to be reduced than $–NO_2$.[64]

Li *et al.*[65] reported the synthesis of functionalized core-shell MXene composites made by a layer-by-layer (LbL) self-assembly strategy via amine-containing polyethyleneimine (PEI) and carboxyl-containing polyacrylic acid (PAA), with the general formula MXene–COOH@$(PEI/PAA)_n$@AuNPs (see Fig. 8). The catalytic potential of the following two selected nanocomposites with different shell layers (i.e., MXene–COOH@$(PEI/PAA)_2$@AuNPs and MXene–COOH@$(PEI/PAA)_{10}$@AuNPs) was investigated for catalytic reduction of 2-nitrophenol (2-NA) and 4-nitrophenol (4-NP). The composites revealed remarkable stability and repeatability (see Table 1, entries 1–4). Based on previous results reported a few years ago,[66] the obtained nanocomposites suspension was added to 2-NA or 4-NP with a fresh $NaBH_4$ mixture. After 8 consecutive cycles, the MXene–COOH@$(PEI/PAA)_{10}$@AuNPs showed enhanced stability and catalytic properties than its MXene–COOH@$(PEI/PAA)_2$@AuNPs counterpart, with less LbL assembled shell structures, indicating the importance of LbL self-assembly for the improvement of porous structures and anchored sites on the surface.

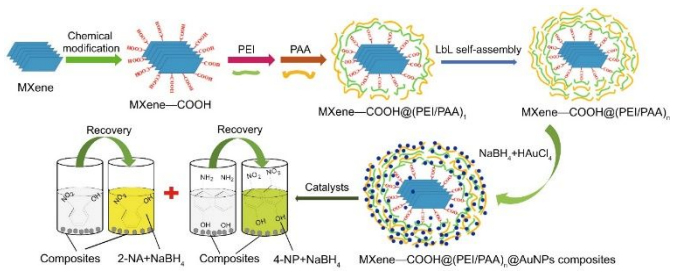

Fig. 8 Graphic design of synthesis and catalysis of MXene–COOH@(PEI/PAA)$_n$@AuNPs nanocomposites. Reproduced with permission from Ref. [65], Copyright 2018 Elsevier.

Fan *et al.*[52] used Pd/alk–$Ti_3C_2X_2$ (alk=alkaline) as catalysts for the hydrogenation of 4-nitrophenol (4-NP) to 4-aminophenol (4-AP) in an aqueous solution.

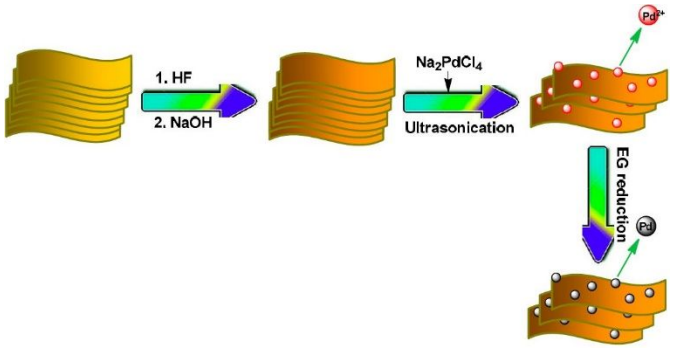

Fig. 9 Schematic representation of the procedure synthesis of Pd/alk–$Ti_3C_2X_2$. Reproduced from Ref. [52] (open access).

The Pd/alk–$Ti_3C_2X_2$ synthesis is described in Fig. 9, and the method used provides well dispersed active sites of Pd on the alk–$Ti_3C_2X_2$ surface. This good dispersion in turn is responsible for the complete conversion and selective hydrogenation of 4-NP to 4-AP in 70 min. Additionally, the catalyst is stable showing no significant loss of catalytic efficiency after seven cycles, making it a promising candidate for numerous catalytic applications.

Noble metals like Pd are intensively used in catalysis.[67,68] Therefore, Xie *et al.*[69] described the synthesis of Pd/$Ti_3C_2T_x$ encapsulated in 3D graphene networks, henceforth referred to as Pd/$Ti_3C_2T_x$⊂graphene hydrogels, as potent and easily retrievable catalysts for efficient hydrogenation of 4-nitroaniline (4-NA) to *p*-phenylenediamine (PPD) in the presence of $NaBH_4$ as the reducing agent. The reaction is quite fast - 91% conversion after 1 min of reaction (see Fig. 10a) - demonstrating that the porous structure of the 3D Pd/$Ti_3C_2T_x$⊂graphene hydrogel is key for the accessibility of active sites for catalytic applications (see Table 1, entries 6–11).

Moreover, this hydrogel was tested for selective hydrogenation reactions with many other nitroaromatic molecules (e.g., 4-chloronitrobenzene, 4-bromonitrobenzene, 4-nitrotoluene, 4-nitrophenol) in order to prove the generality of this catalyst. The results (Fig. 10b) show that this catalyst results in exceptional catalytic performance with high conversion values for all these different nitro-compounds, mostly for those with electron donating functional groups (such as –CH_3 and –OH) compared to molecules with electron withdrawing substituents (i.e. –Cl, –Br) under the same reaction conditions.

Furthermore, it has been shown that the hydrogel is stable after successive recycle tests for the catalytic hydrogenation of 4-NA (see Fig. 10c).

To compare the results obtained with Pd/$Ti_3C_2T_x$⊂graphene hydrogel, Xie *et al.*[69] also prepared Pd/$Ti_3C_2T_x$ films deposited on the poly–vinylidene fluoride (PVDF) substrates. In this case, the conversion of 4-NA over Pd/$Ti_3C_2T_x$ catalyst was 63% after 1 min of reaction, which was much lower than the 91% obtained for Pd/$Ti_3C_2T_x$⊂graphene hydrogel. The integrity of Pd/$Ti_3C_2T_x$ films was preserved during the catalytic processes due to sodium ions and water intercalation into the $Ti_3C_2T_x$ layers, also reported in other studies.[70]

In a recent study, Trandafir *et al.*[71] explored the use of MAX phases as supports for Pd nanoparticles (NPs), at remarkably low concentrations, for the chemoselective hydrogenation of a functionalized nitro-compounds.

The new generation of Pd NPs supported on Ti_3SiC_2 catalysts used in selective hydrogenation reaction of 4-NS achieved a high value of turnover frequency (TOF) of 4.7 × 10^3 h^{-1}, that represents roughly a 100-fold increase over the most selective catalyst known to date (see Fig. 11a). 4-AS is the main product sought here, but other reaction products were identified (i.e., 4-ethylnitrobenzene (4-EN), 4-ethylaniline (4-EA)) depending on the reaction pathway (see Fig. 11b).

Different Pd supporting methods were explored (wet impregnation, deposition-precipitation, mechanical mixing) and the authors found that the number of accessible sites appears to depend on the preparation method.

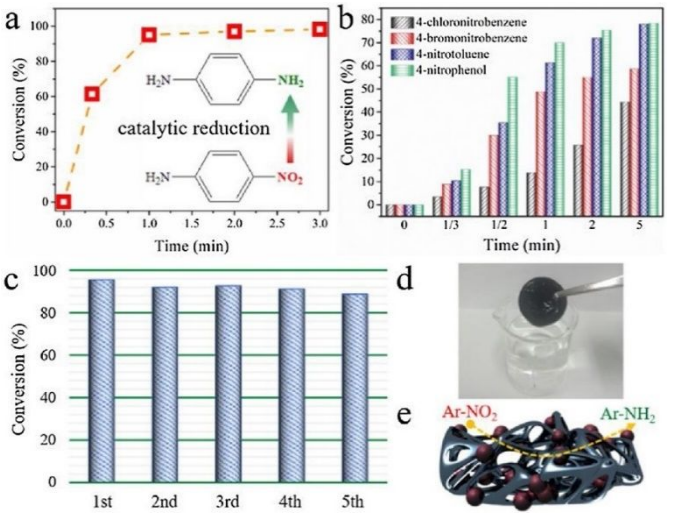

Fig. 10 Catalytic performance of the Pd/$Ti_3C_2T_x$⊂graphene hydrogel for, ***a)*** hydrogenation of 4-NA; ***b)*** hydrogenation of other nitroderivates; ***c)*** Cycling performance for the 4-NA dehydrogenation; ***d)*** Picture of catalyst after hydrogenation reaction; ***e)*** Schematic illustration of the catalytic dehydrogenation reaction. Reproduced with permission from Ref. [69], Copyright 2020 Elsevier.

This journal is © The Royal Society of Chemistry 20xx

Please do not adjust margins

REVIEW

Table 1 Catalytic performance of MAX phases and MXenes-based catalysts in hydrogenation reactions of nitro-compounds.

Entry	Catalyst	Reactant	Conv. [%]	Selectivity [%]	Reaction time	Reducing agent	Ref.
1	MXene–COOH@$(PEI/PAA)_2$@AuNPs	2-Nitrophenol	70 (8 cycles)	-	60 min	-	65
2	MXene–COOH@$(PEI/PAA)_2$@AuNPs with fresh $NaBH_4$	4-Nitrophenol	74 (8 cycles)	-	57 min		
3	MXene–COOH@$(PEI/PAA)_{10}$@AuNPs with fresh $NaBH_4$	2-Nitrophenol	~90 (8 cycles)	-	36 min		
4	MXene–COOH@$(PEI/PAA)_{10}$@AuNPs with fresh $NaBH_4$	4-Nitrophenol	~90 (8 cycles)	-	30 min		
5	Pd/alk–$Ti_3C_2X_2$ in aqueous solution	4-Nitrophenol	99.9	100	70 min	H_2	52
6	Pd/$Ti_3C_2T_x$⊂graphene hydrogels	4-Nitroaniline	91	-	1 min	$NaBH_4$	69
7	Pd/$Ti_3C_2T_x$ films on poly(vinylidene fluoride) (PVDF) substrate	4-Nitroaniline	62.9	-	1 min		
			~80	-	2 min		
			~98	-	5 min		
8	Pd/$Ti_3C_2T_x$⊂graphene hydrogels	4-chloronitrobenzene	~15	-	1 min		
			~25	-	2 min		
			~45	-	5 min		
9	Pd/$Ti_3C_2T_x$⊂graphene hydrogels	4-bromonitrobenzene	~48	-	1 min		
			~55	-	2 min		
			~60	-	5 min		
10	Pd/Ti_3C_2Tx⊂graphene hydrogels	4-nitrotoluene	~63	-	1 min		
			~72	-	2 min		
			~78	-	5 min		
11	Pd/Ti_3C_2Tx⊂graphene hydrogels	4-nitrophenol	~70	-	1 min		
			~75	-	2 min		
			~79	-	5 min		
12	Ti_3SiC_2	4-nitrostyrene	<1	100	24 h	H_2 1.1 MPa	71
			3	100		H_2 2.5 MPa	
13	Ti_2AlC	4-nitrostyrene	<1	100		H_2 1.1 MPa	
			1	100		H_2 2.5 MPa	
14	Ti_3AlC_2	4-nitrostyrene	<1	100		H_2 1.1 MPa	
			4	13		H_2 2.5 MPa	
15	0.05 wt.% Pd/Ti_3SiC_2	4-nitrostyrene	100	0	24 h	H_2	71
16	0.0005 wt.% Pd/Ti_3SiC_2	4-nitrostyrene	100	0		H_2	
17	0.0005 wt.% Pd/Ti_3SiC_2_DP	4-nitrostyrene	100	25		H_2	
18	Pd/Ti_3SiC_2_mix1	4-nitrostyrene	4	100		H_2	
19	Pd/Ti_3SiC_2_mix2	4-nitrostyrene	59 (cycle 1)	73		H_2	
			100(cycle 2)	93			
21	Pd/Ti_3SiC_2_mix3	4-nitrostyrene	100	58		H_2	
22	Pd/Ti_3SiC_2_mix4	4-nitrostyrene	100	10		H_2	
23	Pd/TiC_mix2	4-nitrostyrene	100 (cycle 1)	-		H_2	
			18 (cycle 2)	-			
25	Pd/Ti_2AlC_mix2	4-nitrostyrene	52	27		H_2	
26	Pd/Ti_3AlC_2_mix2	4-nitrostyrene	100	-		H_2	
27	Pd/$Ti_3C_2T_z$_mix2	4-nitrostyrene	90 (cycle 1)	-		H_2	
			25 (cycle 2)	-			

REVIEW

Table 1 (Continued)

Entry	Catalyst	Reactant	Conv. [%]	Selectivity [%]	Reaction time	Reducing agent	Ref.
29	Pd/Ti_3SiC_2_mix2	3-nitrostyrene	100	96	24 h	H_2	[71]
		cinnamaldehyde	94	3 (cinnamyl alcohol)			
				80 (hydro-cinnamaldehyde)			
		trans-β nitrostyrene	9	13			
		4-nitrophenol	18	83			
30	Ni/Ti_3SiC_2	4-nitrostyrene	1	100	24 h	H_2	[71]
31	Pt/$Ti_3C_2T_x$-D-AB	4-chloronitrobenzene	100[1]	99.5	1 h	H_2	[72]
			94[2]	92.4			
			99.8[3]	95.2			
			96.9[4]	92.9			
			2.6[5]	67			
			98.2[6]	95			
			78.1[7]	90.8			
			39.3[8]	83.3			
32	Pt/$Ti_3C_2T_x$-D-SB	4-chloronitrobenzene	40.4[1]	84.3			
33	Pt/$Ti_3C_2T_x$-D-AB	2-chloronitrobenzene	100[1]	96.5	1.5 h		
34	Pt/$Ti_3C_2T_x$-D-AB	3-chloronitrobenzene	100[1]	95.8	2 h		
35	Pt/$Ti_3C_2T_x$-D-AB	4-nitrotoluene	100[1]	98.2			
36	Pt/$Ti_3C_2T_x$-D-AB	2-nitrotoluene	100[1]	94.7			
37	Pt/$Ti_3C_2T_x$-D-AB	2-methoxi-1-nitrobenzene	100[1]	95.7	3 h		
38	Pt/$Ti_3C_2T_x$-D-AB	4-nitrophenol	100[1]	97.4	1.5 h		
39	Pt/$Ti_3C_2T_x$-D-AB	2-fluoronitrobenzene	100[1]	94.7			
40	Pt/$Ti_3C_2T_x$-D-AB	nitrobenzene	100[1]	99.2	1 h		

Reaction conditions: ethanol/water mixture with a volume percent of [1] 28% (total volume: 7.0 mL); [2] 14%; [3] 42%; [4] 56%; [5] 100%; methanol/water mixture with a volume percent of [6] 28%; propanol/water mixture with a volume percent of [7] 28%; 1,4-dioxane/water mixture with a volume percent of [8]28%.

Actually, a good dispersion is obtained using a deposition-precipitation method compared with the large clusters formed through the impregnation method that consequently, limited access to the active sites. Diluting the Pd content by mechanically mixing of impregnated Pd samples with Ti_3SiC_2 was a good strategy to better control the Pd amount. A total conversion of 4-NS with a selectivity of 93% to 4-AS was obtained with an optimal loading of very well dispersed 130 ppm Pd. The authors also showed that higher Pd loadings resulted in selectivity losses. The high chemoselectivity of the Pd/MAX phase catalyst can be assigned to the synergetic effect between the Pd nanoparticle size and dispersion and also to the non-Ti containing oxides (viz. presence of SiO_2 as one of the native oxides formed on the Ti_3SiC_2 phase, the other being titania) that preferentially activate the nitro group. The proof of concept was realised by using the best material as catalyst for different substrates (see Table 1 entries 12–30).

Additionally, Pt nanoparticles on $Ti_3C_2T_x$-based MXene as efficient catalysts have also been investigated recently [72] for selective hydrogenation of *p*-chloronitrobenzene (*p*-CNB) to *p*-chloroaniline (*p*-CAN) (see Fig. 12b). Using ammonia borane (AB) as a mild reducing agent compared with sodium borohydride (SB), highly dispersed and nano-sized metallic Pt crystallites were uniformly decorated on $Ti_3C_2T_x$ nanosheets

(see Fig. 12a). It was concluded that the reducing agent strongly influenced the particle size and distribution of the Pt NPs on the $Ti_3C_2T_x$-D surface. It is remarkable that this catalyst can catalyse the complete conversion of p-CNB with 99.5% selectivity to p-CAN, which is a superior catalytic activity to that of Pt/$Ti_3C_2T_x$-D-SB synthesized with SB (see Table 1, entries 31–32). The excellent performance of Pt/$Ti_3C_2T_x$-D-AB can be assigned to the well-dispersed Pt nanoparticles, abundant surface electron-efficient Pt(0) and also to the synergistic catalysis between hydrophilic Pt/$Ti_3C_2T_x$-D-AB and water (used as co-solvent).

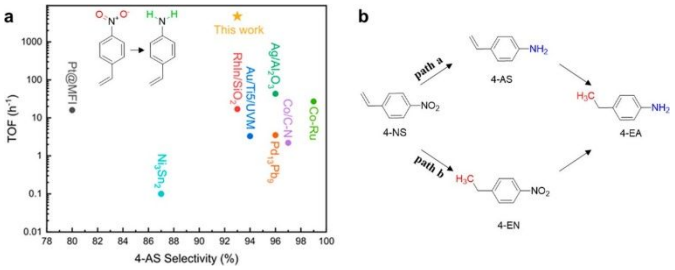

Fig. 11 a) Comparison of the highest TOF values reported in the literature for catalysts in 4-NS hydrogenation to 4-AS, and **b)** Reaction pathways for the hydrogenation reaction of 4-NS.Reproduced with permission from Ref.[71], Copyright 2020 American Chemical Society.

The Pt/$Ti_3C_2T_x$-D-AB catalyst was relatively stable for six cycles, after which it began to deactivate due to Pt aggregation as confirmed by TEM.

Chen *et al.*[72] also tested Pt/$Ti_3C_2T_x$-D-AB in the hydrogenation of a series of nitroaromatic compounds to their corresponding amines with high efficiency (see Table 1, entries 33–40), with conversions that reached 100% in 1–3 h. The target products' selectivity is higher than 94% in all tests which indicates that Pt/$Ti_3C_2T_x$-D-AB is a flexible catalyst that can be used to obtain a series of aromatic amines.

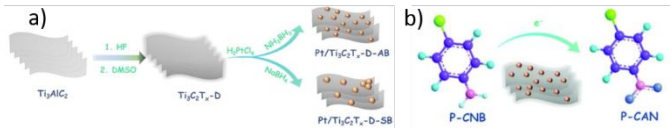

Fig. 12 a) Schematic representation of preparation process of Pt/$Ti_3C_2T_x$-D samples with different reducing agents; **b)** Overview of selective hydrogenation reaction of p-CNB to p-CNA with Pt–MXene based catalysts. Reproduced with permission from Ref. [72], Copyright 2020 Royal Society of Chemistry.

Furfural hydrogenation. During the last decade, an increased attention on selective biomass transformation has occurred. One of the most promising molecule platform derived from hemicelluloses[73] is furfural, mainly considering the value added chemicals obtained by different catalytic reaction such as furfuryl alcohol.

Recently, Naguib *et al.*[74] reported on the catalytic activity of $Ti_3C_2T_x$ and Ti_3CNT_x MXenes for the hydrogenation of furfural to furfuryl alcohol with the scope to understand the role of the presence of nitrogen in the support for carbonyl hydrogenation. Both catalysts had similar activities (36–42%) and selectivities (49–52%). It is worth mentioning that these results are similar or superior when compared with TiO_2, metal carbides or other noble metal-free catalysts under the same conditions. The main difference between $Ti_3C_2T_x$ and Ti_3CNT_x was observed in terms on stability; Ti_3CNT_x was stable for six consecutive runs compared with $Ti_3C_2T_X$ which deactivated faster. This behaviour was explained by the differences of surface terminations, which varied as a function of MXene composition. $Ti_3C_2T_X$ it is richer in surface terminations (especially OH) facilitating the intercalation of the reaction between the layers (leading to faster deactivation). The presence of nitrogen in Ti_3CNT_x significantly lowered the OH terminations and hindered the interaction of the surface with the reactants.

DFT calculation were performed to elucidate the furfural hydrogenation mechanism for Ti_3CNT_x. Apparently, TiO–H Bronsted acid sites present on MXene surface, bind the furfural molecule by C=O functional group, which is further hydrogenated via addition of the hydride dissociated on the metallic active site.

The bifunctionality of MXenes given by the presence of both, metal and OH terminations which act as acids, render these materials quite interesting for a wide range of catalytic reactions. Also, this study revealed, that the surface terminations can have an influence on material stability, and suggests that MXenes surfaces can be tuned in order to target certain reactions.

4. Catalytic degradation

4.1. Short overview

Pharmaceuticals and nonsteroidal anti-inflammatory drugs are used intensively for the treatment of human and animal diseases. The vast majority of drugs used end up in wastewater or ground waters, and removing or destroying them becomes a very difficult task due to their low or non-biodegradability.[75] Similar to pharmaceuticals, also dyes often end up polluting water systems and their removal represents a subject of major interest. Dyes are used in many industries and the most common are methylene blue, Rhodamine B, Methyl orange or Congo red.

Like dyes, pesticides can cause negative impact on humans and animals due to their toxic characteristics. For example, 2,4-dichlorophenoxyacetic acid was frequently found in drinking water in high concentrations due to its high solubility. The development of methods to remove this material from the environment is of great importance because its presence can cause endocrinal disturbance and chromosomal mutations in human lymphocytes. It can also endanger aquatic life.[76]

MAX phase and MXene-based heterojunction materials have been shown to be effective catalysts in the degradation of organic compounds such as pharmaceuticals,[75,77,78] dyes,[79,80] pesticides[76] and other compounds (see Scheme 4).[81,82]

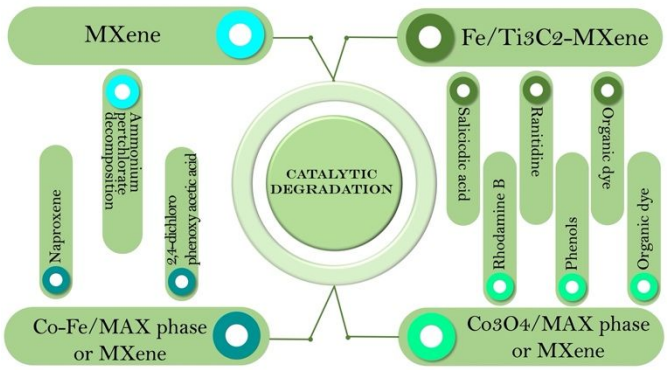

Scheme 4. Types of MAX phase and MXene used in catalytic degradation reactions.

4.2. Ti_3C_2–MXenes modified with iron compounds

Ding *et al.*[77] described the synthesis of a novel nanocomposite catalytic material obtained by supporting α-Fe_2O_3 NPs onto multi-layered Ti_3C_2, and its use as heterogeneous activator of peroxymonosulfate (PMS) for the degradation of salicylic acid. Salicylic acid is a phenolic compound, widely used in the pharmaceutical, cosmetics and food industries. Due to the fact that it has been detected constantly in environmental water systems and it represents a potential threat for ecological systems and humans, various methods to eliminate it from the aqueous environment have been developed. The authors claim that MXenes were selected for supporting α-Fe_2O_3 nanoparticles because of the presence on the surface of different termination groups such as –O, –OH, which provide better aqueous dispersibility and strong anchoring of the free cations through electrostatic interaction.[77]

Three types of nanocomposites were synthesized, FM-1, FM-2, FM-3, using different concentration of $FeCl_3{\cdot}6H_2O$ of 0.5M, 1M and 2M, respectively. The α-Fe_2O_3/MXene nanocomposites presents high efficiency and stability during the activation process of PMS to produce free radicals for the degradation of salicylic acid in aqueous solutions. In neutral conditions, the removal of the salicylic acid was ≈ 97% using FM-2 catalyst nanocomposite. The catalytic system FM-2/PMS displayed low dissolution of metal ions and reusability during five successive runs. A possible mechanism of PMS activation was proposed by the authors based on EPR spectra, quenching tests, XPS and the *in-situ* Raman characterization.

Fig. 13 describes the mechanism which involves, 4 steps. Salicylic acid is degraded by the reactive radicals generated during the PMS activation process. Unfortunately, the known instability of MXenes in water was not taken into account.

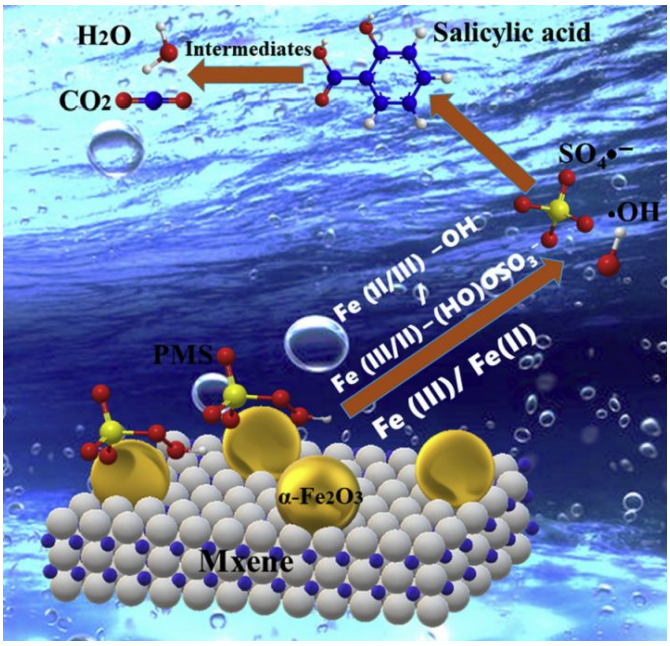

Fig. 13 Schematic diagram of possible mechanism of PMS activation by FM nanocomposite. Reprinted with permission from Ref. [77], Copyright 2020 Elsevier.

Another example of drugs present in aquatic systems, that require their removal from water is ranitidine, due to its carcinogenic effect. Ranitidine is frequently used as a histamine H_2-receptor antagonist and is utilized for the treatment of ulcers and gastroesophageal reflux, due to the presence of furan rings in its structure.[78]

Zang *et al.*[78] reported obtaining magnetic zero-valent iron (nZVI)@Ti_3C_2-based MXene nanosheets *via* an *in situ* reductive deposition, which efficiently succeed in degrading ranitidine in the presence of H_2O_2, a Fenton-like process. (see Fig. 14) The proposed mechanism for catalytic degradation of ranitidine in the presence of H_2O_2 and (nZVI)@Ti_3C_2-based MXene nanosheets (see Fig. 14) could be divided in five steps: (i) molecules of ranitidine diffuse and are adsorbed at the surface of the (nZVI)@Ti_3C_2 nanosheets; (ii) the nZVIPs undergo oxidative corrosion; (iii) cyclic transformation of ≡Fe(III)/≡Fe(II) occurs; (iv) ferrous iron activates H_2O_2 molecules; (v) hydroxyl radicals react with ranitidine. In this scheme the Ti_3C_2-based MXene plays the role of a cathode, favouring a direct electron transfer reaction. The nZVI cores behave as an electron donors and the iron-based oxide outer shell promotes a series of ≡Fe(III)/≡Fe(II) conversions.

Apart from drug removal, a Fenton-like catalyst, Fe_3O_4/Ti_3C_2–MXene proved to be efficient also in organic dye degradation. Zang *et al.* [80] developed, for the first time, a one-pot synthesis method for magnetic MXene composites (Ti_3C_2-MNPs) which incorporated Fe_3O_4 nanoparticles into Ti_3C_2 nanosheets via thermal treatment (see Fig. 15).

This journal is © The Royal Society of Chemistry 20xx

Please do not adjust margins

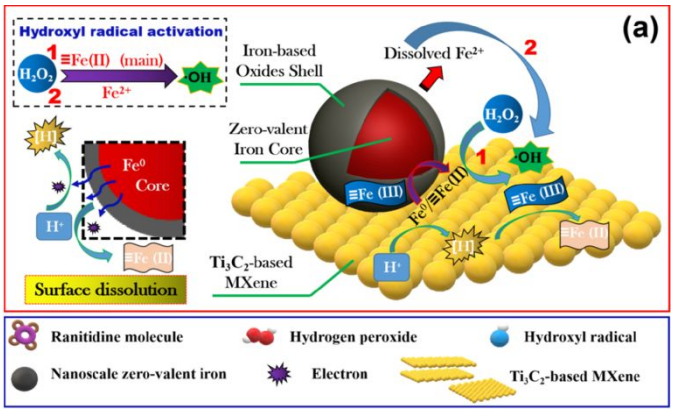

Fig. 14 Schematic of the mechanism of ranitidine catalytic degradation by (nZVI)@Ti_3C_2/H_2O_2 system. Reprinted with permission from Ref. [78], Copyright 2021 Elsevier.

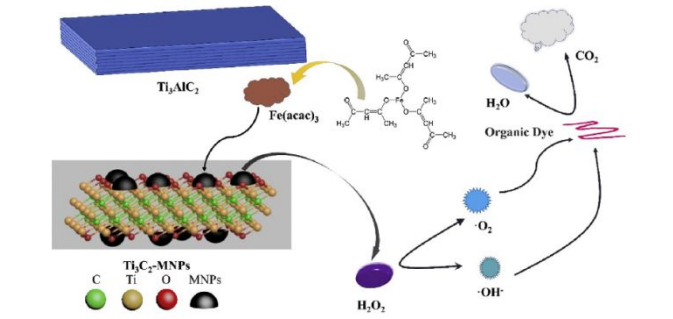

Fig. 15 Schematic for the synthesis of Ti_3C_2/Fe_3O_4 system and their utilisation in dyes degradation (reproduced with permission from Ref. [80], Copyright 2020 Elsevier.

The hybrid Ti_3C_2/Fe_3O_4 system presents high degradation efficiency of organic dyes. The optimal conditions occur at pH=3, a catalyst concentration and H_2O_2 concentration are 0.5 g L^{-1} and 10 mmol/L, respectively, at a temperature = 40 °C. The degradation mechanism involves the presence of hydroperoxyl radicals (•OH) and superoxide radicals ($O_2^{\bullet-}$) radicals that are formed due to the presence in the system of H_2O_2.[80] Here again H_2O_2 is a very oxidizing agent and whether the MXene flakes would survive for times that are useful for an application has to be carefully considered.

4.3. MAX phase and MXenes modified with Co_3O_4

As in the case of Fe, Co also degraded organic dyes or phenols when it was deposited on MXenes and the MAX phases. Thus, nanocomposites of Co_3O_4 particle-modified MXene (MXene-Co_3O_4) synthesized by solvothermal method showed good performance for catalytic degradation of methylene blue and Rhodamine B (see Fig. 16).[79] The capacity of MXene-Co_3O_4 to degrade methylene blue and Rhodamine B can be attributed to the positive synergistic effect of MXene, dye and Co_3O_4 in the presence of H_2O_2. Cationic dye molecules were adsorbed on the MXene surfaces due to electrostatic attraction and this process increased the concentration of dye molecules anchored on the surface of MXene-Co_3O_4 leading to a high catalytic degradation rate. Also, the hydrophilicity of MXene facilitate the dispersion of MXene-Co_3O_4 in water and improved the contact between molecules and H_2O_2 was effectively catalyzed to produce free OH radical species that promoted dye degradation.[79]

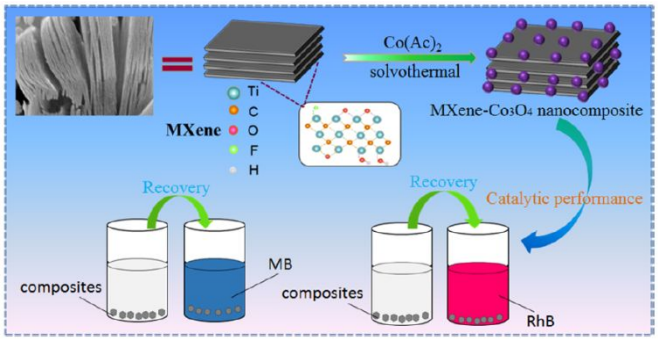

Fig. 16 Schematic representation for the synthesis of Ti_3C_2/Co_3O_4 system and catalytic process of dyes degradation. Reprinted with permission from Ref. [79], Copyright 2021 American Chemical Society.

Wang *et al.*[81] reported the synthesis of sandwiched $Co_3O_4/Ti_3C_2T_x$ composites as heterogeneous catalyst to activate PMS for Bisphenol A catalytic degradation, another toxic compound for humans and animals, released from polymers in fabrication of water bottles, sport equipment, coatings of food containers, etc.[83] The Co_3O_4/ $Ti_3C_2T_x$ composites were obtained by impregnation and the highest catalytic activity was obtained when the loading of Co_3O_4 was about 20% on $Ti_3C_2T_x$ (see Fig. 17). In addition, Co_3O_4/Ti_3AlC_2 composites activates PMS in a wide range of pH (4–10) and shows good catalytic performance with the existence of anions such as NO_3^- and Cl^-. Oxidizing species detected in the Co_3O_4/ $Ti_3C_2T_x$ /PMS system were $SO_4^{\bullet-}$ and •OH radicals.

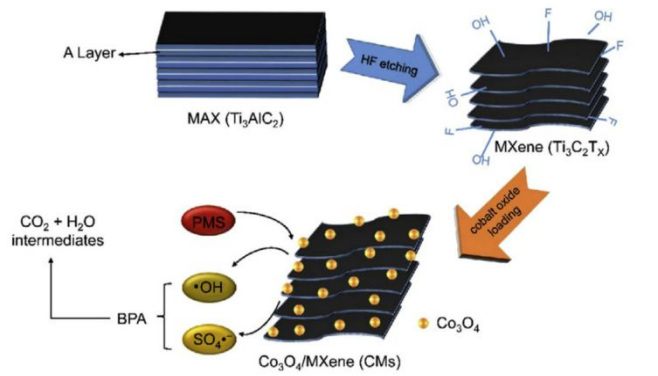

Fig. 17 Schematic for the synthesis of Ti_3AlC_2/Co_3O_4 system and their utilisation in BPA catalytic degradation. Reprinted with permission from Ref. [81], Copyright 2018 Elsevier.

4.4. MAX phase and MXenes modified with iron and cobalt

The high activity of Fe and Co supported on the MAX phases and MXenes presented in catalytic degradation, encouraged the researchers to continue and explore also the synergy between the two elements (Fe and Co). Park *et al.*[75] described the synthesis of a heterogeneous nanocomposite catalyst of MXene nanosheets (synthesized from Ti_3AlC_2) functionalized with $CoFe_2O_4$ nanoparticles that can be used for the activation of persulfate (PS) to degrade naproxen in water. Naproxen is a nonsteroidal anti-inflammatory drug used in the treatment of

rheumatoid arthritis and acute muscle pain[75] and similar to salicylic acid, it contaminates environmental water systems and its removal represents a subject of major interest.

The experiments described by the authors confirm that neither $CoFe_2O_4$ nanoparticles nor MXenes alone can activate PS, but the $CoFe_2O_4$@MXene system proved to be an efficient catalyst for PS activation. A proposed mechanism for naproxen degradation with persulfate activated by this nanohybrid system is described in Fig. 18.

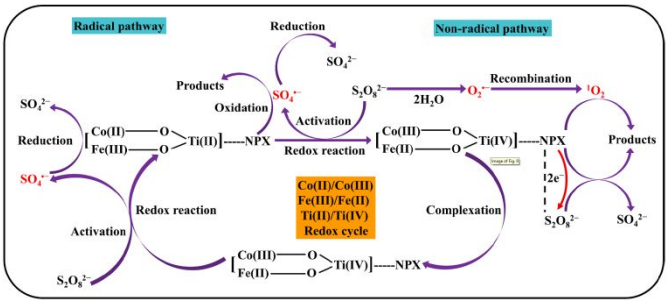

Fig. 18 Proposed mechanism for naproxen degradation with PS activated by $CoFe_2O_4$@MXene. Reprinted with permission from Ref. [75], Copyright 2021 Elsevier.

Coordination interactions of Co and Fe moieties with MXene functional groups modulate redox reactions of stable Co/Fe/Ti couples. The electrons are transferred from PS to form $SO_4^{\bullet-}$ /$S_2O_8^{\bullet-}$ by thermodynamically oxidation of Co(II)/Fe(II)/Ti(II) and reduction of Co(III)/Fe(III)/Ti(IV). By activating PS with $CoFe_2O_4$@MXene, radical reactive spices such as •OH, $SO_4^{\bullet-}$, $O_2^{\bullet-}$ and the corresponding nonradical $^1O_2$ are formed, which significantly promotes naproxen degradation.

Moreover, the naproxen adsorbed on the $CoFe_2O_4$@MXene acts as an electron donor and transfers two electrons to PS that is, in turn, reduced to $2SO_4^{2-}$. Naproxen was degraded approximately 99% in the presence of PS at 1 g L^{-1} of $CoFe_2O_4$@MXene dosage.

Composite such as $Fe_2CoTi_3O_{10}$-MXene were described by Xie *et al.*[76] as heterogeneous catalyst for oxidative degradation of 2,4-dichlorophenoxyacetic acid based on PMS activation. These composites could efficiently activate PMS and, under neutral conditions, approximately 98% of 2,4-dichlorophenoxyacetic acid was removed. In the catalytic oxidation process, radicals such as •OH, $SO_4^{\bullet-}$ are generated and the main activation mechanism for PMS can be represented by the electron transfer between the PMS and ternary transition metals (Fe, Co and Ti) active sites on the catalyst surface.[76]

It is our duty to warn the readers that the catalytic degradations presented in the sections 4.1-4.4, that are using Ti-based MXenes, are useful from academic/fundamental point of view, showing some synergetic effects between the supported Fe and Co transition metals and the Ti-based MXene. Unfortunately, Ti-based MXenes, are not stable in water for a long time, therefore any practical applications are not feasible.

In addition, when studying the Fenton degradation of drugs in aquatic systems, researchers should take into account that the use of H_2O_2 will also result in faster MXenes oxidation and their transformation in to metal oxides will occur.

4.5. MXenes for ammonium perchlorate decomposition

Recently, *Jiao et al.* [82] have shown that Ti_3C_2 has intrinsic catalytic activity for the thermal decomposition of ammonium perchlorate-based molecular perovskites such as $[(H_2dabco)[NH_4(ClO_4)_3]$. Experiments revealed that adding 10 wt.% Ti_3C_2 in the reaction mixture reduced the decomposition temperature by 43.8 °C at a heating rate of 10 °C·min^{-1}.

The catalytic mechanism (Fig. 19) proposed by the authors assumed that the thermal decomposition of ammonium perchlorate-based molecular perovskite is mainly determined by the stability of the cage-like framework structures of the substrate which were composed of NH_4^+ cations and ClO_4^- anion.[82]

The inherent catalytic properties of MXene can realise thermal decomposition of ammonium perchlorate-based molecular perovskite by lowering the decomposition temperature, activated energy, and more heat release.[82]

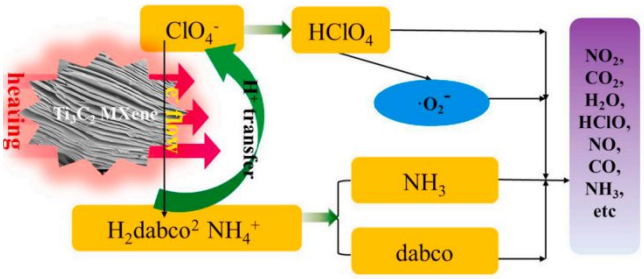

Fig. 19 Schematic of catalysis decomposition mechanism of $[(H_2dabco)[NH_4(ClO_4)_3]$ with Ti_3C_2 MXene. Reprinted with permission from Ref. [82], Copyright 2020 Elsevier.

Along the same lines, Cu_2O supported on Ti_3C_2 MXene was found to provide a higher catalytic activity compared with Ti_3C_2 MXene or Cu_2O alone, in the thermal decomposition of ammonium perchlorate (AP).[84] Combining the advantages of Cu_2O and MXene, good thermal conductivity, improved heat transfer rate of reaction system and also high surface areas and lamellar structure of MXene, thermal decomposition temperature of ammonium perchlorate was significantly reduced by 121.4 °C compared to that of the pure AP.

This year, Li *et al.*[85] demonstrated that Ti_3C_2 MXene-supported CuO nanocomposites also significantly decrease the decomposition temperature of AP from 425.0 °C for pure AP to 324.9 °C and increase the exothermic heat from 295.2 J g^{-1} of pure ammonium perchlorate to 1272.9 J g^{-1} in the presence of MXene-supported CuO nanocomposites.

These results prove that the MXene used as support for CuO or Cu_2O could be a viable solution to enhance the catalytic performance in ammonium perchlorate decomposition, which is of major interest.

5. Applications of MXenes in photocatalysis

5.1. Short overview

Photocatalysis can be described as the acceleration of a photoreaction in the presence of a catalyst, called

This journal is © The Royal Society of Chemistry 20xx

Please do not adjust margins

photocatalyst, that is often stable to the photolysis conditions and attains a large number of oxidative conversions per active site without significant degradation of its redox catalytic capacity.[86] In the case of heterogeneous photocatalysis, upon photoexcitation of several semiconductor photocatalysts nonhomogeneously suspended in either aqueous or nonaqueous solutions or in gaseous mixtures, the photogenerated electron-hole pairs migrate to the external surface and initiate simultaneous oxidation and reduction reactions.[86,87] Depending on the reaction media, the photogenerated electrons and holes might interact directly with the adsorbate's molecules (e.g., the photocatalytic overall water splitting reaction) or create reactive species (e.g., hydroxyl and superoxide radicals) that undergo non-selective oxidative processes to break down different substances including organic materials, pesticides, dyes or bacteria, among others.[88]

The major hurdle that needs to be overcome in this area is the recombination of photogenerated electrons and holes. In this regard, the combination of MXenes with various semiconductor photocatalysts led to a marked increase in photoactivity. Such phenomena are caused by the structural merits of MXenes including: (i) abundant hydrophilic groups (–OH and –O) present on the external surfaces that afford considerable interaction with various semiconductors to form composite heterostructured photocatalysts; (ii) strong redox activities of surface metallic sites (e.g., Ti, Nb or V) existing on the MXene surfaces which are greater than the redox reactivity of carbon materials,[89] and (iii) due to their metallic character, MXenes possess excellent electron conductivity that guarantees efficient charge transport.[90]

As typical representative among MXene materials, $Ti_3C_2T_x$ features high electrical conductivity, surface hydrophilicity, and tuneable electronic properties that makes it a suitable co-catalyst in various photocatalytic applications. Thus, benefitting from the Schottky effect (due to the high work functions of $Ti_3C_2T_x$ 3.9–4.8 eV depending on the surface termination in comparison with most well-established semiconductor photocatalysts)[91] and the accompanying built-in electric field, the photogenerated charges of several semiconductors interfaced with $Ti_3C_2T_x$ can be effectively separated and, from a photocatalytic point of view, this process enhances the activity of the photocatalytic system.

Bearing an excellent metallic conductivity (the measured conductivity of single-layer $Ti_3C_2T_x$ was reported to be up to 6.76 × 10^5 S m^{-1}, which is comparable to that of graphene films that is situated in the range 5 × 10^6 to 6.4 × 10^6 S m^{-1}),[92,93] MXenes can boost the activity of semiconductor photocatalysts. In comparison with graphene, however, the use of MXenes as co-catalyst brings several advantages.[94,95] For instance, in the construction of graphene-based semiconductor photocatalysts, the majority of the literature data report the use of graphene oxide (GO) followed by a reduction processes to generate reduced graphene oxide (RGO).[96] The adoption of this synthesis route causes a significant loss in electronic conductivity due to the presence of numerous point defects and the reported electrical conductivity of RGO (<1 × 10^3 S m^{-1})[97] is about two orders of magnitude below the conductivity of $Ti_3C_2T_x$. Another interesting discovery shows that MXenes can serve as hole acceptors during the photocatalytic reactions, a fact that was never reported in the case of graphene-based semiconductor photocatalysts.[94]

On the other hand, $Ti_3C_2T_x$ use as co-catalyst comes with a big disadvantage: its low stability in water. However, within the formed photocatalytic composite, the $Ti_3C_2T_x$ should not be seen as the Trojan horse, since the oxidized product is TiO_2, which itself possess excellent photoactivity. Moreover, as will be shown later in Tables 2-4, the stability and the photoactivity of the photocatalyst composite obtained by *in situ* approach (e.g., solvothermal procedure) is significantly greater than that obtained by the electrostatic self-assembly process.

The application of $Ti_3C_2T_x$ in the field of photocatalysis is summarized in this review by following four aspects: i) photocatalytic hydrogen, H_2, evolution reactions (HER) through water splitting, ii) photocatalytic carbon dioxide, CO_2, reduction reactions (CO_2RR), iii) photocatalytic degradation reactions of various pollutants, and iv) nitrogen photofixation and other photocatalytic/photo-assisted processes (see Scheme 5). As many reviews were recently published on this topic,[11–14] here we only report on studies published in the last two years. Moreover, the aim of this section is not to provide an exhaustive review of this area, but to present general aspects to be considered, and then to outline which are currently the most efficient photocatalytic systems comprising $Ti_3C_2T_x$.

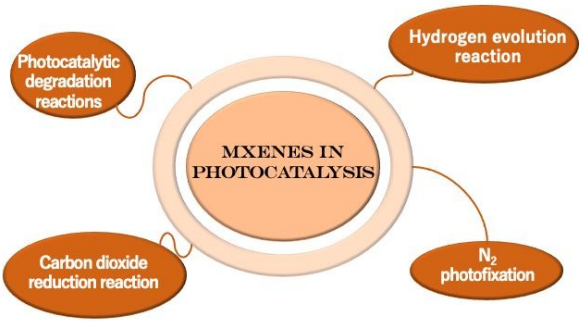

Scheme 5. MXenes in photocatalysis.

5.2. Applications in hydrogen evolution reaction

As stated above, after photogeneration, the electron-hole pairs initiate simultaneous oxidation and reduction reactions at the outer surfaces of the photocatalyst. In order to maintain charge neutrality during the photocatalytic process, the consumption rate of electrons and holes must be equal. For this reason, most of the studies on HER are carried out with an excess of electrons donor reagents.[98] Thus, while the holes are quenched and used by different hole scavengers, the electrons reduce the H^+ species followed by the formation of intermediate adsorbed H* states and finally the production of H_2 molecules.[99]

In the field of H_2 generation through photocatalytic water splitting, the first synthesized MXene, $Ti_3C_2T_x$, is also the most widely used because it forms Schottky junctions that promote the separation of photogenerated charge carriers. Beside this,

the DFT calculated Gibbs free energy for atomic H adsorption on the surface of O-terminated Ti_3C_2 ($|\Delta G_{H^*}|$=0.00283 eV)[89] is much lower than that of the highly active and well-known HER catalyst, Pt ($\Delta G_{H^*}\approx$-0.09 eV)[100] and thus much closer to the most desired $|\Delta G_{H^*}|$, value which should be zero[99].

Table 2 Comparison of photocatalysts $Ti_3C_2T_x$ MXene in hydrogen evolution reaction.[a]

Photocatalyst	Preparation methods	Reaction conditions	Light source	Sacrificial reagent	H_2 production [μmol g^{-1} h^{-1}]	AQY [%]	Ref.
$Pt/ZnIn_2S_4/Ti_3C_2T_x$ (3 wt.% Pt)	Solvothermal procedure	20 mg catalyst dispersed in 40 mL TEOA (10 v.%)	300 W Xe lamp (λ ≥ 400 or 420 nm)	TEOA	6,482 (≥ 400 nm) 3,475 (≥ 420 nm)	20.41 (400 nm) 11.14 (420 nm)	105
Chlorophyll-$Ti_3C_2T_x$	Electrostatic self-assembly process	3 mg catalyst dispersed in 3 mL AA (55 mM)	350 W Xe lamp (λ ≥ 400 nm)	AA	52	np	106
MXene@Au@CdS	Stepwise approach	4 mg catalyst dispersed in 80 mL sacrificial agent aqueous solution	300 W Xe lamp (λ ≥ 420 nm)	0.25 M Na_2SO_3 and 0.35 M Na_2S	17,070.43	np	107
TiO_2–Ti_3C_2/Ru	Stepwise approach	10 mg catalyst dispersed in 80 mL methanol (10 v.%)	300 W Xe lamp (350–780 nm)	Methanol	235.3	14.33 (350 nm)	108
p-g-$C_3N_4/Ti_3C_2T_x$	Electrostatic self-assembly process	40 mg catalyst dispersed in 60 mL TEOA (10 v.%)	300 W Xe lamp	TEOA	982.8	np	109
$CdLa_2S_4/Ti_3C_2$	Hydrothermal procedure	50 mg catalyst dispersed in 100 mL sacrificial agent aqueous solution	300 W Xe lamp (λ ≥ 420 nm)	0.25 M Na_2SO_3 and 0.35 M Na_2S	11,182.4	15.6 (420 nm)	110
$BiVO_4$@$ZnIn_2S_4$/ Ti_3C_2	Ultrasonic assisted self-assembly process	60 mg catalyst	300 W Xe lamp (λ ≥ 420 nm)	No scavenger	102.67	2.9 (460 nm)	111
g-C_3N_4/Ti_3C_2	Stepwise approach	50 mg catalyst dispersed in 100 mL TEOA (10 v.%)	300 W Xe lamp (λ ≥ 420 nm)	TEOA	116.2	np	112
CdS@Ti_3C_2@CoO	Stepwise approach	20 mg catalyst dispersed in 100 mL DI	300 W Xe lamp (λ ≥ 420 nm)	No scavenger	134.46	np	113
2 wt.%Pt/ UCN/$Ti_3C_2T_x$/BQD	Stepwise approach	10 mg catalyst in 78 mL TEOA (10 v.%)	300 W Xe lamp (λ ≥ 420 nm)	TEOA	18,420	17.6 (420 nm)	101
$Cd_{0.5}Zn_{0.5}S/Ti_3C_2$	Hydrothermal procedure	50 mg catalyst dispersed in 100 mL DI or seawater	300 W Xe lamp (λ ≥ 420 nm)	0.25 M Na_2SO_3 and 0.35 M Na_2S	9.07	43.28 (420 nm, DI splitting and AM 1.5G)	114
1 wt.%Pt/ HCN/Ti_3C_2	Ionothermal method	20 mg catalysts dispersed in 100 mL TEOA (10 v.%)	3 W led lamp (420 nm)	TEOA	4,225	14.6 (420 nm)	115
CdS nanorods/$Ti_2C_3T_x$	Hydrothermal procedure	20 mg catalyst dispersed in 100 mL TEOA (20 v.%)	300 W Xe lamp	TEOA	63.53	2.28	116
TiO_2-C/CdS synthesized from Ti_3C_2/CdS	Calcination	50 mg catalysts dispersed in 100 mL lactic acid (20 v.%)	300 W Xe lamp (λ ≥ 420 nm)	Lactic acid	1,480	np	102
0.5 wt.% Pt/TiO_2@C synthesized from Ti_3C_2	Calcination	35 mg catalyst dispersed in 100 mL TEOA (10 v.%)	Solar simulator AM 1.5G	TEOA	160.42	np	103

[a] Results included in studies published starting from 2020 onwards only; AA: ascorbic acid; UCN: ultrathin carbon nitride; BQD: black phosphorus quantum dots; TEOA: triethanolamine; DI: deionized water; HCN: heptazine-based crystalline carbon nitride; np: information not provided by authors.

Table 2 summarizes several examples of $Ti_3C_2T_x$-based photocatalysts used in the most recent years for HER. The synthetic approaches to combine different semiconductor photocatalysts with $Ti_3C_2T_x$ and several reaction parameters are also presented. These reports demonstrated that $Ti_3C_2T_x$ could greatly improve the photoactivity compared to solely the base photocatalyst. The highest H_2 production activity and apparent quantum efficiency (AQE) of 18.42 mmol h^{-1} g^{-1} and 17.6% (at 420 nm), respectively, was obtained when Ti_3C_2 nanosheets were mixed with ultrathin 0D/2D black phosphorus/ultrathin carbon nitride heterojunctions that was loaded with 2 wt.%Pt

This journal is © The Royal Society of Chemistry 20xx

Please do not adjust margins

and tested in the photocatalytic water splitting in the presence of triethanolamine as a hole scavenger.[101]

Besides its role of co-catalyst, $Ti_3C_2T_x$ can be used as precursor for the generation of TiO_2-based active photocatalysts through a simple thermal degradation process.[102,103] Thus, flash oxidation of 2D $Ti_3C_2T_x$ in air resulted in the formation of a hybrid structure of thin sheets of disordered graphitic carbon decorated with nanocrystalline anatase.[104] In this regard, Table 2 presents two of the most recent experiments comprising the use of $Ti_3C_2T_x$ as precursor for obtaining photocatalysts with remarkable photoactivity toward HER (see refs. [92] and [93]).

5.3. Applications in carbon dioxide reduction reaction, CO_2RR

In comparison with the photocatalytic water splitting, the photocatalytic reduction of CO_2 is a much more complicated process, due to several aspects which include but are not limited to the following: (i) although water is the most suitable hydrogen donor for CO_2 reduction, in aqueous solutions, HER competes with CO_2RR; (ii) while basic pH increases CO_2 solubility in water, this is not necessarily advantageous since, under these conditions, the real species that are present would be carbonates or bicarbonates, which are more difficult to reduce than CO_2 itself and, in this way, the advantages of high solubility, meaning high concentration of substrate around the photocatalyst is lost; (iii) performing CO_2RR under gas phase conditions might lead to the formation of less volatile reaction products that can strongly adsorb or deposit on the photocatalysts surface and act as poisons; (iv) in the cases in which the concentration of CO_2RR products is low, the impurities (e.g., adsorbed airborne organic compounds) present on the surface of the photocatalyst might lead to misleading results concerning the real activity of the photocatalysts.[117]

Considering all these difficulties, it is not surprising that the number of studies on CO_2RR are much less than those on water splitting. More importantly, the instability of MXene's carbon atoms causing interferences during the CO_2RR limits the application of $Ti_3C_2T_x$-based photocatalysts in CO_2RR in comparison with its use for photocatalytic water splitting.

As shown in Table 3, among the limited reports in recent years, as co-catalyst, $Ti_3C_2T_x$ promotes the separation of charge carriers leading to the formation of solely C1 products (i.e., CO and CH_4), while the lack of C2 products (e.g., formaldehyde, formic acid or oxalic acid) formation indicates that $Ti_3C_2T_x$ cannot change the energy barrier of the base photocatalyst.

A great enhancement of the photoactivity toward CO_2RR was obtained by Que *et al.*[118] by anchoring an inorganic halide perovskite $FAPbBr_3$ (formamidinium lead bromide) quantum dots on Ti_3C_2 nanosheets to form a $FAPbBr_3/Ti_3C_2$ composites within a Schottky heterojunction. Thus, under visible light irradiation, an optimal electron consumption rate of 717 μmol $g^{-1}h^{-1}$ is obtained, which corresponds to a ≈ 2 -fold improvement over pristine $FAPbBr_3$ QDs (344 μmol g^{-1} h^{-1}).

Table 3 Comparison of photocatalysts $Ti_3C_2T_x$ MXene in carbon dioxide reduction reaction.[a]

Photocatalyst	Preparation methods	Reaction conditions	Light source	Products and yield [μmol g^{-1} h^{-1}]	Ref.
$FAPbBr_3/Ti_3C_2$	Deposition	3 mg catalyst, 0.5 mL deionized water and CO_2 (1 bar)	300 W Xe lamp (λ ≥ 420 nm)	283.41 (CO) 17.7 (CH_4)	118
$Cu_2O/Ti_3C_2T_x$	Hydrothermal procedure	30 mg catalyst coated onto a quartz plate and CO_2 (<1 atm)	300 W Xe lamp	17.5 (CO) 1.0 (CH_4)	119
$g\text{-}C_3N_4/Ti_3C_2T_x$	Calcination	50 mg catalysts uniformly dispersed on a 28.26 cm^2 glass sheet, 5 mL water and 1 mL CO_2 gas	300 W Xe lamp	2.1 (CH_4) 4 (CO)	120
$g\text{-}C_3N_4/TiO_2/C$ synthesized from $Ti_3C_2T_x$	Electrostatic self-assembly and calcination	Certain amounts of catalyst and water. CO_2 (cca. 1 atm)	arc Xe lamp	8.65 (CO) 1.23 (CH_4)	121

[a] Results included in studies published starting from 2020 onwards only.

5.4. Applications in photocatalytic degradation reactions

Degradation of both atmospheric and aquatic organic contaminants can be efficiently performed through heterogeneous photocatalysis. Here the photocatalytic degradation process follows three main steps: (i) photogeneration of electron-hole pairs upon light irradiation; (ii) formation of highly active radicals (i.e., •OH, $O_2^{\bullet-}$, and HOO•) onto the surface as a result charge separation, and (iii) redox processes initiated by these radicals.

While the photogenerated holes react with surface bound water molecules or hydroxyl groups (OH^-) to produce the hydroxyl radical (•OH), photogenerated electrons interact with oxygen and generate anionic superoxide radical ($O_2^{\bullet-}$). These are the most common radicals formed at the surface of photocatalysts, with the hydroperoxyl radical (HOO•) being produced through a $O_2^{\bullet-}$ protonation process.

The •OH radicals are extremely powerful oxidizing agents that initiate a non-selective oxidative attack over the adsorbed organic molecules or those that are close to the photocatalyst surface, causing them to mineralize to an extent depending upon their structure and stability level.[122] On the other hand, the $O_2^{\bullet-}$ radicals not only initiate further oxidation processes but also prevent charge recombination.

REVIEW

Table 4 Comparison of photocatalysts $Ti_3C_2T_x$ MXene in photocatalytic degradation reactions.[a]

Photocatalyst	Preparation methods	Reaction conditions	Light source	Substrate of degradation	Oxygenic species	Removal rate/rate constants [%]/[min^{-1}]	Ref.
ZnO-Ti_3C_2	Ultrasonic assisted self-assembly process	35 mg catalyst dispersed in 50 mL RhB (10 mg L^{-1})	300 W Xe lamp (λ ≥ 420 nm)	RhB	np	98 / 0.0077	133
$Bi_2WO_6/C_3N_4/Ti_3C_2$	Hydrothermal procedure	30 mg catalysts dispersed in 200 mL CIP (10 mg L^{-1}).	300 W Xe lamp	CIP	h^+ / $O_2^{\bullet-}$	0.058	134
$TiO_2(TiO_{2-x})/Ti_3C_2$	Stepwise synthesis	5 mg catalysts dispersed in 50 mL BPA (15 mg L^{-1}),	300 W Hg lamp (λ < 365 nm)	BPA	•OH / $O_2^{\bullet-}$	90.5	135
Ti_3C_2/Ti^{3+}-TiO_2	Stepwise synthesis	100 mg catalyst coated on a glass slide. Continuous flow (20 sccm) of acetaldehyde (500 ppm)	500 W Xe lamp (λ ≥ 420 nm)	acetaldehyde	•OH / $O_2^{\bullet-}$	27	136
α-$Fe_2O_3/ZnFe_2O_4$@Ti_3C_2	Ultrasonic assisted self-assembly process	20 mg catalyst dispersed in 100 mL RhB (10 mg L^{-1}) or Cr(VI) (10 mg L^{-1})	300 W Xe lamp (λ ≥ 400 nm)	RhB Cr(VI)	$O_2^{\bullet-}$ / h^+ / e^-	~98 / 0.02686	137
Ti_3C_2/TiO_2	Solvothermal procedure	20 mg catalyst dispersed in 50 mL RhB (20 mg L^{-1})	300 W Xe lamp	RhB	h^+	93.7	138
TiO_2/g–C_3N_4 synthesized from Ti_3C_2	Calcination	60 mg catalysts dispersed in 100 mL of pollutants: TC (15 mg L^{-1}); CIP (3 mg L^{-1}); BPA (5 mg L^{-1}); RhB (20 mg L^{-1})	300 W Xe lamp (λ ≥ 400 nm)	TC CIP BPA RhB	$O_2^{\bullet-}$ / •OH	0.02442 0.01675 0.01935 0.05586	139
BiOBr/$TiO_2/Ti_3C_2T_x$	Hydrothermal procedure	20 mg catalyst dispersed in 50 mL RhB	300 W Xe lamp (λ ≥ 420 nm)	RhB	•OH / $O_2^{\bullet-}$	99.8	140
Ti_3C_2/TiO_2/BiOCl	Solvothermal procedure	50 mg catalyst dispersed in 50 mL RhB (10 mg L^{-1}) or TC (20 mg L^{-1})	500 W Xe lamp AM 1.5G	RhB TC	$O_2^{\bullet-}$ / •OH	84 / 0.0143 0.0157	141
$TiO_2/Ti_3C_2T_x$	Solvothermal procedure	certain amount of catalyst dispersed in 100 mL MO	500 W Hg lamp	MO	np	92	142
$Ti_3C_2/BiPO_4$	Hydrothermal procedure	100 mg catalyst dispersed in 50 mL RhB (10 mg L^{-1})	300 W Xe lamp (λ ≥ 420 nm)	RhB	$O_2^{\bullet-}$ / •OH	100/0.12469	143
ZnO/Ti_3C_2	Hydrothermal procedure	50 mg catalyst dispersed in 200 mL MB (10 mg L^{-1})	40 W Hg lamp (365 nm)	MB	$O_2^{\bullet-}$ / •OH	83.97 / 0.03357	144
Ti_3C_2/TiO_2	Hydrothermal oxidation method	certain amount of atalyst (200 mg L^{-1}) and PFOA (20 μM)	Hg lamp (254 nm)	PFOA	np	99.9	145
CoAl-LDHs/$Ti_3C_2T_x$	Electrostatic self-assembly process	100 mg catalyst dispersed in 100 mL TCH	300 W Xe lamp (λ ≥ 420 nm)	TCH	$O_2^{\bullet-}$ > h^+ > •OH	96.67	146
Ag/Ag_3PO_4/Ti_3C_2	Electrostatic self-assembly process	50 mg catalyst dispersed in 100 mL MO (20 mg L^{-1}) 40 mg catalyst dispersed in 80 mL Cr(VI) (10 mg L^{-1})	300 W Xe lamp (λ ≥ 420 nm)	MO Cr(VI)	h^+, e^- h^+, e^-	93 / 0.044 61 / 0.014	147

REVIEW

Table 4 (Continued)

Photocatalyst	Preparation methods	Reaction conditions	Light source	Substrate of degradation	Oxygenic species	Removal rate/rate constants [%]/[min^{-1}]	Ref.
TiO_2/Ti_3C_2	Stepwise synthesis	40 mg catalyst dispersed in 50 mL RhB (20 μM)	Solar simulator AM 1.5G	RhB	$•OH > O_2^{•-}$	95	148
$CaIn_2S_4/Ti_3C_2T_x$	Hydrothermal procedure	50 mg catalyst dispersed in 50 mL TCH (20 mg L^{-1}) or Cr(VI) (20 mg L^{-1})	400 W metal halogen lamp (λ ≥ 420 nm)	TCH Cr(VI)	$O_2^{•-}$ / h^+ e^-	96 98	149
Sm-g-C_3N_4/Ti_3C_2	Stepwise synthesis	20 mg catalyst dispersed in 100 mL CIP (20 mg L^{-1})	300 W Xe lamp (λ ≥ 420 nm)	CIP	$O_2^{•-}$ / h^+	99	150
$BiOBr/Ti_3C_2$	Solvothermal procedure	10 mg catalyst dispersed in 50 mL RhB (20 mg L^{-1})	300 W Xe lamp (λ ≥ 420 nm)	RhB	$O_2^{•-}$	99.3 / 0.23043	151
iN-Ti_3C_2/TiO_2	Stepwise synthesis	10 mg catalyst dispersed in 50 mL MB (20 mg L^{-1})	300 W Hg lamp (λ < 365 nm)	MB	•OH	0.02642	152
$WO_3/Ti_3C_2/In_2S_3$	Ultrasonic assisted self-assembly process	5 mg catalyst dispersed in 10 mL BPA (10 mg L^{-1}) 10 mg catalyst dispersed in 20 mL Cr(VI) (20 mg L-1)	30 W Xe lamp	BPA Cr(VI)	$O_2^{•-}$ e^-	97.6 99.8	153
$NiCo_2S_4/Ti_3C_2$	Hydrothermal procedure	5 mg catalyst dispersed in 50 mL RhB (50 mg L^{-1})	250 W Xe lamp (400–800 nm)	RhB	$O_2^{•-}$/ •OH	100	154
$Ti_3C_2/SnNb_2O_6$	Ultrasonication-assisted hydrothermal method	15 mg catalyst dispersed in 60 mL TCH (10 mg L^{-1}) and RhB (10 mg L^{-1})	300 W Xe lamp (λ ≥ 420 nm)	TCH RhB	•OH h^+	70 / 0.0145 98 / 0.0579	155
Ti_3C_2/Ag_2S	Ultrasonic assisted self-assembly process	50 mg catalyst dispersed in 100 mL MB (20 mg L^{-1}) 50 mg catalyst dispersed in 50 mL mixed dyes (20 mg L^{-1} each): MB, MO, MR, RhB	300 W Xe lamp (λ ≥ 420 nm)	MB MB RhB MO MR	$O_2^{•-} > e^- > h^+ > •OH$	98 / 0.08222 99.2 / 0.99198 99.54 / 0.99538 96.98 / 0.96985 87.45 / 0.87451	156
ZnS/Ti_3C_2	Ultrasonic assisted self-assembly process	35 mg catalyst dispersed in 50 mL RhB (10 mg L^{-1})	300 W Xe lamp (λ ≥ 420 nm)	RhB	np	0.02464	157

[a] Results included in studies published starting from 2020 onwards only; RhB: rhodamine B; CIP: ciprofloxacin; BPA: bisphenol A; TC: tetracycline; PMS: peroxymonosulfate; DCF: diclofenac; MO: methyl orange; TCH: tetracycline hydrochloride; iN: isopropyl amine modified; MB: methylene blue; PFOA: perfluorooctanoic acid; MR: methyl red; np: information not provided by authors.

It should be noted that during the photocatalytic degradation processes, the inherent presence of oxidative radicals in the reaction medium, the UV light irradiation and the photothermal effect induced by the near-infrared irradiation may oxidize the $Ti_3C_2T_x$ surfaces.[94,123] On the other hand, the target dye molecules (especially the cationic ones) can be adsorbed on the MXene surfaces and might change/affect their surface and electronic states.[124,125] In this regard, it is clear that the reactions and interactions between $Ti_3C_2T_x$ and the aqueous environment are complicated and more detailed investigations (preferably operando and in situ) are needed to reveal the true working mechanism of the photocatalytic degradation processes on the surface of MXenes-based composites.

As shown in Table 4, the photocatalytic degradation reactions of various pollutants (e.g., methylene blue, methyl orange, bisphenol A, rhodamine B, diclofenac, tetracycline or tetracycline hydrochloride, among others) or the removal of toxic metals (i.e., reduction of Cr (VI) anions) from water are the most studied applications of $Ti_3C_2T_x$-based photocatalysts. Once again, the introduction of $Ti_3C_2T_x$ within a photocatalytic composite improves the photoactivity mainly due to the promotion of the separation of charge carriers and the presence

of a wealth of surface groups and active sites where the targeted molecules are easily adsorbed.

5.5. Applications in N_2 photofixation and other photocatalytic/photo-assisted processes

In addition to the photocatalytic applications presented above, there are many other cases in which $Ti_3C_2T_x$, is used as a co-catalyst in photocatalytic systems for different reduction and oxidation processes, like N_2 reduction reaction,[126–129] photocatalytic bireforming of methane,[130] NO oxidation[131] or photo-assisted organic transformations,[132] among others.

The N_2 reduction reaction (NRR) under light irradiation, a process known as N_2 photofixation, has been investigated over different $Ti_3C_2T_x$-based materials. Thus, Huo *et al.*[127] recently developed a highly active photocatalyst toward near-infrared light-driven N_2 photofixation by fabricating a plasmonic hybrid $Ti_3C_2T_x/TiO_2$ structure. The photocatalytic system attained a NH_3 production rate of 422 μmol g^{-1} h^{-1} under full-spectrum irradiation. The authors demonstrate also that oxygen vacancies found on the surface served as the active centers for the adsorption and the activation of N_2 gas molecules.

By using $Ti_3C_2T_x$ as precursor, Qian *et al.*[128] synthesized, through an one-step calcination approach, oxygen vacancy-rich C/TiO_2 materials that showed remarkable activity for NRR. Thus, by using H_2O and CH_3OH as proton sources they were able to produce NH_3 at rates of 41 μmol g^{-1} h^{-1} and 84 μmol g^{-1} h^{-1}, respectively. Once again, the importance of oxygen vacancies in the efficiency of N_2 adsorption and activation was revealed by electron spin-resonance spectroscopy, ESR, and temperature programmed desorption of nitrogen, N_2-TPD, experiments which showed that the chemisorption of N_2 is much more efficient on the surface of C/TiO_2 possessing higher concentrations of oxygen vacancies than in the case of commercial TiO_2.

On the same topic, Gao *et al.*[129] report the performance of NRR over $Ti_3C_2T_x/TiO_2$/Co composite synthesized by introducing Co into the MXene@TiO_2 catalysts in which the TiO_2 nanoparticle derived from the *in situ* growth on the surface of MXene nanosheets. The optimal photocatalyst (containing 0.5 wt.% Co) shows a NH_4^+ production rate of 110 μmol g^{-1} h^{-1} without the addition of any hole scavengers and under UV-Vis light irradiation conditions.

The photocatalytic bireforming of CH_4 under visible light irradiation over Ti_3C_2 nanosheets coupled with a 2D g-C_3N_4/TiO_2 heterojunction was investigated by Khan *et al.*[130] The authors demonstrate that the as-prepared photocatalytic composite show CO and H_2 production rates of 48.4 and 83.2 μmol g^{-1}, reaching apparent quantum yields as high as 0.41 and 0.7 %, respectively.

Another example of the use of gas phase photocatalysis over $Ti_3C_2T_x$-based composites is the photocatalytic oxidation of nitric oxide (NO). In this research line, Li *et al.*[131] report the use of a Ti_3C_2/g-C_3N_4 composites with an enhanced photocatalytic NO removal efficiency. Thus, the authors performed the photocatalytic oxidation of NO and through monitoring by *in situ* diffuse reflectance infrared spectroscopy, they demonstrate that the final products were nitrite and nitrate instead of the undesired and toxic NO_2.

Visible-light induced one-pot hydrogenation and amidation of nitroaromatics with carboxylic acids was recently investigated by Jiang *et al.*[132] The authors prepared Pt/N-TiO_2/Ti_3C_2 heterojunctions by *in situ* growth of TiO_2 on Ti_3C_2 nanosheets and then N doped the TiO_2 with melamine, followed by deposition of Pt nanoparticles. Thus, by using the 3 wt.%Pt/N-TiO_2/Ti_3C_2 photocatalyst and in the presence of K_3PO_4 additive, hydrogenation and amidation reaction of nitrobenzene with acetic acid reached 100% conversion with 100 % chemoselectivity to acetanilide.

6. Concluding remarks

In this review we have shown that the MAX phases and MXenes, with different chemical compositions, can be considered as potential catalysts, as well as supports, creating a synergy with various active species. In some cases, their catalytic activity was similar, or even better, compared with the ones of noble metals containing catalysts, highlighting, once again, their catalytic capabilities. At the current stage, these materials are proving to be extremely promising in various catalytic applications, however their surface chemistry and thermal stability are not fully understood.

At this time MXenes cannot be applied in industrial processes, as their large-scale production is not yet possible due to the HF involved in the synthesis, that cannot be used in large quantities. Progress is expected on the synthesis method to avoid the use of HF, so that the remarkable properties observed for these materials in heterogeneous catalytic reactions can go further, to make possible their industrialization.

Depending on the application, these materials have been shown to be extremely resistant to coke, or if deactivation has been observed, it has been much slower than in the case of standard catalysts. One of the best ways to counter-part this issue is by tuning the chemical compositions and surface terminations.

Finally, we would like to draw attention to the two subclasses of these materials that have not yet been explored in heterogeneous catalytic reactions, other than electrochemical ones, namely double M'M''AX phase, obtained by alloying MAX phase with another metal, and i-MXenes (in plan ordered MXenes).[158] Usually, alloying of a MAX phase with another metal leads to chemically disordered solid solutions, that can be an advantage in catalytic applications which are depended on surface defects. Likewise, in the case of i-MXene, the etching process results in 2D MXene structures with ordered vacancies, ordered divacancies or disordered vacancies with a huge potential in catalytic applications.[158] The development of these materials is still in its infancy, but we predict a rapid evolution, because the presence of vacancies and how they can influence the properties of the final catalytic material, not only that is scientifically rewarding for any researchers, but has major implications in the development of new materials for a variety of practical applications.

This journal is © The Royal Society of Chemistry 20xx

Please do not adjust margins

As compared with the oxides-based catalysts, MAX phase and MXenes have been narrowly investigated as catalysts in traditional heterogeneous processes. However, further theoretical and experimental concerted studies, will pave the way for new heterogenous applications, such as selective oxidation of different hydrocarbons to added value compounds, but also in total oxidation reactions. Furthermore, appropriate modification of their surface, or intercalation between the layers of different chemical compounds, will open new avenues for MAX phase and MXenes to be used as heterogenous catalysts. (e.g., oxidative coupling of amines to imines).

Lastly a word of caution: MXenes are unstable in aqueous environments in which there is dissolved oxygen. In some cases, the oxidation occurs by hydrolysis[123] and thus reducing dissolved oxygen does not solve the problem. There are ways to mitigate oxidation[159,160] but whether such approaches solve the long-term problem, especially in an open system, is an open question at this time. If this problem is not solved and/or shown not to be an issue, then all the work in that domain will be totally academic with no practical applications. Along the same lines and somewhat ironically, it follows that oxidizing the MXenes to their more stable oxides and possibly C[104] as some have done, may be an advisable and fruitful way forward.

Summarizing, it is clear that there is room for improvement in the design and synthesis of MAX phase and MXene based catalysts and in this regard several strategies can be adopted, such as tuning the chemical compositions, ratios between elements, or surface terminations. As shown by the studies presented in this review, the deposition of different chemical species (transition metal oxides, metals) on MAX phase or MXene materials can lead to new different compounds/structures that have never been reported on "classical support", which leads us to believe that these materials are not sufficiently explored, and represent a vast reservoir of both, knowledge and potential applications.

Author Contributions

I. M. C. contributed to Section 3, A. G. M. contributed to Section 4, S. N. contributed to Section 5, while M. F., M. W. B. and F. N. contributed to the remaining sections with scientific writing, illustrations and tables drafting. M. F., M. W. B. and F. N. supervised the research work and contributed with funding acquisition, outline drafting, reviewing, and editing the overall text, illustrations and tables of the manuscript.

Conflicts of interest

There are no conflicts to declare.

Acknowledgements

This work was supported by a grant of the Ministry of Research, Innovation and Digitization, CNCS/CCCDI – UEFISCDI, project number PN-III-P1-1.1-TE-2019-1969, within PNCDI III. MWB acknowledges the support of the Division of Materials Research of NSF (DMR 1740795).

References

1 M. W. Barsoum, *Prog. Solid State Chem.*, 2000, **28**, 201–281.
2 M. Naguib, M. Kurtoglu, V. Presser, J. Lu, J. Niu, M. Heon, L. Hultman, Y. Gogotsi and M. W. Barsoum, *Adv. Mater.*, 2011, **23**, 4248–4253.
3 M. W. Barsoum, *MAX Phases: Properties of Machinable Ternary Carbides and Nitrides*, Wiley-VCH Verlag, 2013.
4 M. Sokol, V. Natu, S. Kota and M. W. Barsoum, *Trends Chem.*, 2019, **1**, 210–223.
5 L. Verger, V. Natu, M. Carey and M. W. Barsoum, *Trends Chem.*, 2019, **1**, 656–669.
6 W. H. K. Ng, E. S. Gnanakumar, E. Batyrev, S. K. Sharma, P. K. Pujari, H. F. Greer, W. Zhou, R. Sakidja, G. Rothenberg, M. W. Barsoum and N. R. Shiju, *Angew. Chemie Int. Ed.*, 2018, **57**, 1485–1490.
7 P. Eklund, M. Beckers, U. Jansson, H. Högberg and L. Hultman, *Thin Solid Films*, 2010, **518**, 1851–1878.
8 Z. M. Sun, *Int. Mater. Rev.*, 2011, **56**, 143–166.
9 P. Eklund, J. Rosen and P. O. Å. Persson, *J. Phys. D. Appl. Phys.*, 2017, **50**, 113001.
10 L. Verger, C. Xu, V. Natu, H.-M. Cheng, W. Ren and M. W. Barsoum, *Curr. Opin. Solid State Mater. Sci.*, 2019, **23**, 149–163.
11 J. K. Im, E. J. Sohn, S. Kim, M. Jang, A. Son, K.-D. Zoh and Y. Yoon, *Chemosphere*, 2021, **270**, 129478.
12 L. Yu, B. Liu, Y. Wang, F. Yu and J. Ma, *J. Power Sources*, 2021, **490**, 229250.
13 Q. Zhong, Y. Li and G. Zhang, *Chem. Eng. J.*, 2021, **409**, 128099.
14 X. Li, Y. Bai, X. Shi, N. Su, G. Nie, R. Zhang, H. Nie and L. Ye, *Mater. Adv.*, 2021, **2**, 1570–1594.
15 Y. Zhang, X. Zhang, C. Cheng and Z. Yang, *Chinese Chem. Lett.*, 2020, **31**, 931–936.
16 C. Yang, H. Huang, H. He, L. Yang, Q. Jiang and W. Li, *Coord. Chem. Rev.*, 2021, **435**, 213806.
17 Z. Xia, Q. Huang and S. Guo, *FlatChem*, 2019, **17**, 100129.
18 M. A. Gibson and J. W. Hightower, *J. Catal.*, 1976, **41**, 420–430.
19 E. H. Lee, *Catal. Rev.*, 1974, **8**, 285–305.
20 G. Busca, in *Heterogeneous Catalytic Materials*, ed. G. Busca, Elsevier, Amsterdam, 2014, pp. 375–419.
21 C. Doornkamp and V. Ponec, *J. Mol. Catal. A Chem.*, 2000, **162**, 19–32.
22 F. Cavani, N. Ballarini and A. Cericola, *Catal. Today*, 2007, **127**, 113–131.
23 J. Diao, M. Hu, Z. Lian, Z. Li, H. Zhang, F. Huang, B. Li, X. Wang, D. S. Su and H. Liu, *ACS Catal.*, 2018, **8**, 10051–10057.
24 J. Diao, Z. Feng, R. Huang, H. Liu, S. B. A. Hamid and D. S. Su, *ChemSusChem*, 2016, **9**, 662–666.
25 D. S. Su, S. Perathoner and G. Centi, *Chem. Rev.*, 2013, **113**,

5782–5816.

26 Z. Li, Y. Cui, Z. Wu, C. Milligan, L. Zhou, G. Mitchell, B. Xu, E. Shi, J. T. Miller, F. H. Ribeiro and Y. Wu, *Nat. Catal.*, 2018, **1**, 349–355.

27 Z. Li, L. Yu, C. Milligan, T. Ma, L. Zhou, Y. Cui, Z. Qi, N. Libretto, B. Xu, J. Luo, E. Shi, Z. Wu, H. Xin, W. N. Delgass, J. T. Miller and Y. Wu, *Nat. Commun.*, 2018, **9**, 5258.

28 B. Qiao, A. Wang, X. Yang, L. F. Allard, Z. Jiang, Y. Cui, J. Liu, J. Li and T. Zhang, *Nat. Chem.*, 2011, **3**, 634–641.

29 X. Sun, Y. Gao, C. Zhao, S. Deng, X. Zhong, G. Zhuang, Z. Wei and J. Wang, *Adv. Theory Simulations*, 2019, **2**, 1800158.

30 A. Kurlov, E. B. Deeva, P. M. Abdala, D. Lebedev, A. Tsoukalou, A. Comas-Vives, A. Fedorov and C. R. Müller, *Nat. Commun.*, 2020, **11**, 4920.

31 C. M. Damaskinos, M. A. Vasiliades and A. M. Efstathiou, *Appl. Catal. A Gen.*, 2019, **579**, 116–129.

32 L. Foppa, M.-C. Silaghi, K. Larmier and A. Comas-Vives, *J. Catal.*, 2016, **343**, 196–207.

33 R. Thakur, A. VahidMohammadi, J. Smith, M. Hoffman, J. Moncada, M. Beidaghi and C. A. Carrero, *ACS Catal.*, 2020, **10**, 5124–5134.

34 Z. Liu, D. C. Grinter, P. G. Lustemberg, T. D. Nguyen-Phan, Y. Zhou, S. Luo, I. Waluyo, E. J. Crumlin, D. J. Stacchiola and J. Zhou, *Angew. Chem., Int. Ed.*, 2016, **55**, 7455.

35 R. Thakur, M. Hoffman, A. VahidMohammadi, J. Smith, M. Chi, B. Tatarchuk, M. Beidaghi and C. A. Carrero, *ChemCatChem*, 2020, **12**, 3639–3643.

36 R. Thakur, A. VahidMohammadi, J. Moncada, W. R. Adams, M. Chi, B. Tatarchuk, M. Beidaghi and C. A. Carrero, *Nanoscale*, 2019, **11**, 10716–10726.

37 M. Ronda-Lloret, V. S. Marakatti, W. G. Sloof, J. J. Delgado, A. Sepúlveda-Escribano, E. V Ramos-Fernandez, G. Rothenberg and N. R. Shiju, *ChemSusChem*, 2020, **13**, 6401–6408.

38 X. Zhang, J. Lei, D. Wu, X. Zhao, Y. Jing and Z. Zhou, *J. Mater. Chem. A*, 2016, **4**, 4871–4876.

39 C. Cheng, X. Zhang, M. Wang, S. Wang and Z. Yang, *Phys. Chem. Chem. Phys.*, 2018, **20**, 3504–3513.

40 Y. Li, Z. Zhou, G. Yu, W. Chen and Z. Chen, *J. Phys. Chem. C*, 2010, **114**, 6250–6254.

41 E. H. Song, Z. Wen and Q. Jiang, *J. Phys. Chem. C*, 2011, **115**, 3678–3683.

42 T.-T. Jia, C.-H. Lu, K.-N. Ding, Y.-F. Zhang and W.-K. Chen, *Comput. Theor. Chem.*, 2013, **1020**, 91–99.

43 J. L. Shi, J. H. Wu, X. J. Zhao, X. L. Xue, Y. F. Gao, Z. X. Guo and S. F. Li, *Nanoscale*, 2016, **8**, 19256–19262.

44 C. Cheng, X. Zhang, Z. Yang and K. Hermansson, *Adv. Theory Simulations*, 2019, **2**, 1900006.

45 H. Oschinski, Á. Morales-García and F. Illas, *J. Phys. Chem. C*, 2021, **125**, 2477–2484.

46 M. Manadé, F. Viñes and F. Illas, *Carbon N. Y.*, 2015, **95**, 525.

47 S. Kim, A. Ruiz Puigdollers, P. Gamallo, F. Viñes and J. Y. Lee, *Carbon N. Y.*, 2017, **120**, 63.

48 S. H. Talib, S. Baskaran, X. Yu, Q. Yu, B. Bashir, S. Muhammad, S. Hussain, X. Chen and J. Li, *Sci. China Mater.*, 2021, **64**, 651–663.

49 E. B. Deeva, A. Kurlov, P. M. Abdala, D. Lebedev, S. M. Kim, C. P. Gordon, A. Tsoukalou, A. Fedorov and C. R. Müller, *Chem. Mater.*, 2019, **31**, 4505.

50 D. Damma, T. Boningari and P. G. Smirniotis, *Mol. Catal.*, 2018, **451**, 20.

51 G. Wang, J. A. Schaidle, M. B. Katz, Y. Li, X. Pan and L. T. Thompson, *J. Catal.*, 2013, **304**, 92.

52 G. Fan, X. Li, C. Xu, W. Jiang, Y. Zhang, D. Gao, J. Bi and Y. Wang, *Nanomaterials*, 2018, **8**, 141.

53 Z. Li and Y. Wu, *Small*, 2019, **15**, 1–10.

54 M. Naguib, M. Kurtoglu, V. Presser, J. Lu, J. Niu, M. Heon, L. Hultman, Y. Gogotsi and M. W. Barsoum, *Adv. Mater.*, 2011, **23**, 4248–4253.

55 M. Naguib, V. N. Mochalin, M. W. Barsoum and Y. Gogotsi, *Adv. Mater.*, 2014, **26**, 992–1005.

56 B. Zielińska, A. Wróblewska, K. Maślana, P. Miądlicki, K. Kiełbasa, A. Rozmysłowska-Wojciechowska, M. Petrus, J. Woźniak, A. M. Jastrzębska, B. Michalkiewicz and E. Mijowska, *Appl. Catal. A Gen.*, 2020, **604**, 117765.

57 J. B. Sharmeen, F. M. Mahomoodally, G. Zengin and F. Maggi, *Molecules*, 2021, **26**, 666.

58 N. Girola, C. R. Figueiredo, C. F. Farias, R. A. Azevedo, A. K. Ferreira, S. F. Teixeira, T. M. Capello, E. G. A. Martins, A. L. Matsuo, L. R. Travassos and J. H. G. Lago, *Biochem. Biophys. Res. Commun.*, 2015, **467**, 928–934.

59 D. Formenti, F. Ferretti, F. K. Scharnagl and M. Beller, *Chem. Rev.*, 2019, **119**, 2611–2680.

60 D. Wang and D. Astruc, *Chem. Rev.*, 2015, **115**, 6621–6686.

61 H.-U. Blaser, C. Malan, B. Pugin, F. Spindler, H. Steinei and M. Studer, *Adv. Synth. Catal.*, 2003, **345**, 103–151.

62 M. Crespo-Quesada, F. Cardenas-Lizana, A.-L. Dessimoz and L. Kiwi-Minsker, *ACS Catal.*, 2012, **2**, 1773–1786.

63 G. Vile, D. Albani, N. Almora-Barrios, N. López and J. Pørez-Ramirez, *ChemCatChem*, 2016, **8**, 21–33.

64 H. U. Blaser, H. Steiner and M. Studer, *ChemCatChem*, 2009, **1**, 210–221.

65 K. Li, T. Jiao, R. Xing, G. Zou, Q. Zhao, J. Zhou, L. Zhang and Q. Peng, *Green Energy Environ.*, 2018, **3**, 147–155.

66 P. Hervés, M. Pérez-Lorenzo, L. M. Liz-Marzán, J. Dzubiella, Y. Lu and M. Ballauff, *Chem. Soc. Rev.*, 2012, **41**, 5577–5587.

67 K. S. Egorova and V. P. Ananikov, *Angew. Chemie - Int. Ed.*, 2016, **55**, 12150–12162.

68 L. Zhang, Z. J. Shao, X. M. Cao and P. Hu, *J. Phys. Chem. C*, 2018, **122**, 20337–20350.

69 X. Xie, Z. Wu and N. Zhang, *Chinese Chem. Lett.*, 2020, **31**, 1014–1017.

70 M. Ghidiu, J. Halim, S. Kota, D. Bish, Y. Gogotsi and M. W. Barsoum, *Chem. Mater.*, 2016, **28**, 3507–3514.

71 M. M. Trandafir, F. Neaţu, I. M. Chirica, Ş. Neaţu, A. C. Kuncser, E. I. Cucolea, V. Natu, M. W. Barsoum and M. Florea, *ACS Catal.*, 2020, **10**, 5899–5908.

72 Q. Chen, W. Jiang and G. Fan, *Dalt. Trans.*, 2020, **49**, 14914–14920.

73 J. P. Lange, E. Van Der Heide, J. Van Buijtenen and R. Price, *ChemSusChem*, 2012, **5**, 150–166.

This journal is © The Royal Society of Chemistry 20xx

Please do not adjust margins

74 M. Naguib, W. Tang, K. L. Browning, G. M. Veith, V. Maliekkal, M. Neurock and A. Villa, *ChemCatChem*, 2020, **12**, 5733–5742.
75 A. Fayyaz, K. Saravanakumar, K. Talukdar, Y. Kim, Y. Yoon and C. Min, *Chem. Eng. J.*, 2021, **407**, 127842.
76 M. Ding, W. Chen, H. Xu, Z. Shen, T. Lin, K. Hu and Q. Kong, *Chem. Eng. J.*, 2019, **378**, 122177.
77 M. Ding, W. Chen, H. Xu, Z. Shen, T. Lin and K. Hu, *J. Hazard. Mater.*, 2020, **382**, 121064.
78 Y. Ma, X. Lv, D. Xiong, X. Zhao and Z. Zhang, *Appl. Catal. B Environ.*, 2021, **284**, 119720.
79 S. Luo, R. Wang, J. Yin, T. Jiao, K. Chen, G. Zou, L. Zhang, J. Zhou, L. Zhang and Q. Peng, , DOI:10.1021/acsomega.9b00231.
80 Y. Cui, M. Liu, H. Huang, D. Zhang, J. Chen and L. Mao, *Ceram. Int.*, 2020, **46**, 11593–11601.
81 Y. Liu, R. Luo, Y. Li, J. Qi, C. Wang, J. Li, X. Sun and L. Wang, *Chem. Eng. J.*, 2018, **347**, 731–740.
82 K. Han, X. Zhang, P. Deng, Q. Jiao and E. Chu, *Vacuum*, 2020, **180**, 109572.
83 L. Zhao, Y. Ji, D. Kong, J. Lu, Q. Zhou and X. Yin, *Chem. Eng. J.*, 2016, **303**, 458–466.
84 Y. Gao, L. Wang, Z. Li, A. Zhou, Q. Hu and X. Cao, *Solid State Sci.*, 2014, **35**, 62–65.
85 K. Li, Y. Lei, J. Liao and Y. Zhang, *Inorg. Chem. Front.*, 2021, **8**, 1747–1761.
86 M. A. Fox and M. T. Dulay, *Chem. Rev.*, 1993, **93**, 341–357.
87 F. Neaţu, L. E. Abramiuc, M. M. Trandafir, R. F. Negrea, M. Florea, C. M. Teodorescu and S. Neaţu, *ChemCatChem*, 2020, **12**, 4642–4651.
88 A. O. Ibhadon and P. Fitzpatrick, *Catalysts*, 2013, **3**, 189–218.
89 J. Ran, G. Gao, F.-T. Li, T.-Y. Ma, A. Du and S.-Z. Qiao, *Nat. Commun.*, 2017, **8**, 13907.
90 H.-J. Lin, Q.-L. Mo, S. Xu, Z.-Q. Wei, X.-Y. Fu, X. Lin and F.-X. Xiao, *J. Catal.*, 2020, **391**, 485–496.
91 T. Schultz, N. C. Frey, K. Hantanasirisakul, S. Park, S. J. May, V. B. Shenoy, Y. Gogotsi and N. Koch, *Chem. Mater.*, 2019, **31**, 6590–6597.
92 X. Sang, Y. Xie, M.-W. Lin, M. Alhabeb, K. L. Van Aken, Y. Gogotsi, P. R. C. Kent, K. Xiao and R. R. Unocic, *ACS Nano*, 2016, **10**, 9193–9200.
93 J. Krupka and W. Strupinski, *Appl. Phys. Lett.*, 2010, **96**, 82101.
94 X. Xie and N. Zhang, *Adv. Funct. Mater.*, 2020, **30**, 2002528.
95 C. Yu, L. Peng, Y. Zhu, G. Xie, Z. Wu, X. Xie and N. Zhang, *J. Mater. Chem. A*, 2021.
96 M.-Q. Yang, N. Zhang, M. Pagliaro and Y.-J. Xu, *Chem. Soc. Rev.*, 2014, **43**, 8240–8254.
97 C. Gómez-Navarro, R. T. Weitz, A. M. Bittner, M. Scolari, A. Mews, M. Burghard and K. Kern, *Nano Lett.*, 2007, **7**, 3499–3503.
98 Ş. Neaţu, M. Puche, V. Fornés and H. Garcia, *Chem. Commun.*, 2014, **50**, 14643–14646.
99 Y. Jiao, Y. Zheng, M. Jaroniec and S. Z. Qiao, *Chem. Soc. Rev.*, 2015, **44**, 2060–2086.
100 B. Hinnemann, P. G. Moses, J. Bonde, K. P. Jørgensen, J. H. Nielsen, S. Horch, I. Chorkendorff and J. K. Nørskov, *J. Am. Chem. Soc.*, 2005, **127**, 5308–5309.
101 T. Song, L. Hou, B. Long, A. Ali and G. J. Deng, *J. Colloid Interface Sci.*, 2021, **584**, 474–483.
102 N. Zhao, Y. Hu, J. Du, G. Liu, B. Dong, Y. Yang, J. Peng, J. Li and M. Zhai, *Appl. Surf. Sci.*, 2020, **530**, 147247.
103 J. Liu, X. Kong, Y. Li, S. Zhu, Y. Liang, Z. Li, S. Wu, C. Chang, Z. Cui and X. Yang, *Appl. Surf. Sci.*, 2020, **530**, 147283.
104 M. Naguib, O. Mashtalir, M. R. Lukatskaya, B. Dyatkin, C. Zhang, V. Presser, Y. Gogotsi and M. W. Barsoum, *Chem. Commun.*, 2014, **50**, 7420–7423.
105 G. Zuo, Y. Wang, W. L. Teo, A. Xie, Y. Guo, Y. Dai, W. Zhou, D. Jana, Q. Xian, W. Dong and Y. Zhao, *Angew. Chemie - Int. Ed.*, 2020, **59**, 11287–11292.
106 Y. Li, X. Chen, Y. Sun, X. Meng, Y. Dall'Agnese, G. Chen, C. Dall'Agnese, H. Ren, S. Sasaki, H. Tamiaki and X. Wang, *Adv. Mater. Interfaces*, 2020, **7**, 1902080.
107 J. Yin, F. Zhan, T. Jiao, W. Wang, G. Zhang, J. Jiao, G. Jiang, Q. Zhang, J. Gu and Q. Peng, *Sci. China Mater.*, 2020, **63**, 2228–2238.
108 Y. Liu, Y.-H. Li, X. Li, Q. Zhang, H. Yu, X. Peng and F. Peng, *ACS Nano*, 2020, **14**, 14181–14189.
109 J. Kang, S. Byun, S. Kim, J. Lee, M. Jung, H. Hwang, T. W. Kim, S. H. Song and D. Lee, *ACS Appl. Energy Mater.*, 2020, **3**, 9226–9233.
110 L. Cheng, Q. Chen, J. Li and H. Liu, *Appl. Catal. B Environ.*, 2020, **267**, 118379.
111 X. Du, T. Zhao, Z. Xiu, Z. Xing, Z. Li, K. Pan, S. Yang and W. Zhou, *Appl. Mater. Today*, 2020, **20**, 100719.
112 J. Li, L. Zhao, S. Wang, J. Li, G. Wang and J. Wang, *Appl. Surf. Sci.*, 2020, **515**, 145922.
113 Z. Ai, K. Zhang, B. Chang, Y. Shao, L. Zhang, Y. Wu and X. Hao, *Chem. Eng. J.*, 2020, **383**, 123130.
114 G. Zeng, Y. Cao, Y. Wu, H. Yuan, B. Zhang, Y. Wang, H. Zeng and S. Huang, *Appl. Mater. Today*, 2021, **22**, 100926.
115 J. Li, J. Li, C. Wu, Z. Li, L. Cai, H. Tang, Z. Zhou, G. Wang, J. Wang, L. Zhao and S. Wang, *Carbon N. Y.*, 2021, **179**, 387–399.
116 B. Sun, P. Qiu, Z. Liang, Y. Xue, X. Zhang, L. Yang, H. Cui and J. Tian, *Chem. Eng. J.*, 2021, **406**, 127177.
117 Ștefan Neațu, J. Maciá-Agulló and H. Garcia, *Int. J. Mol. Sci.*, 2014, **15**, 5246–5262.
118 M. Que, Y. Zhao, Y. Yang, L. Pan, W. Lei, W. Cai, H. Yuan, J. Chen and G. Zhu, *ACS Appl. Mater. \& Interfaces*, 2021, **13**, 6180–6187.
119 J. Zhang, J. Shi, S. Tao, L. Wu and J. Lu, *Appl. Surf. Sci.*, 2021, **542**, 148685.
120 X. Li, Y. Bai, X. Shi, J. Huang, K. Zhang, R. Wang and L. Ye, *Appl. Surf. Sci.*, 2021, **546**, 149111.
121 Y. Yang, D. Zhang, J. Fan, Y. Liao and Q. Xiang, *Sol. RRL*, 2021, **5**, 2000351.
122 A. Ajmal, I. Majeed, R. N. Malik, H. Idriss and M. A. Nadeem, *RSC Adv.*, 2014, **4**, 37003–37026.
123 T. Habib, X. Zhao, S. A. Shah, Y. Chen, W. Sun, H. An, J. L. Lutkenhaus, M. Radovic and M. J. Green, *npj 2D Mater. Appl.*, 2019, **3**, 8.
124 O. Mashtalir, K. M. Cook, V. N. Mochalin, M. Crowe, M. W.

Barsoum and Y. Gogotsi, *J. Mater. Chem. A*, 2014, **2**, 14334–14338.

125 Q. Peng, J. Guo, Q. Zhang, J. Xiang, B. Liu, A. Zhou, R. Liu and Y. Tian, *J. Am. Chem. Soc.*, 2014, **136**, 4113–4116.

126 C. Hao, Y. Liao, Y. Wu, Y. An, J. Lin, Z. Gu, M. Jiang, S. Hu and X. Wang, *J. Phys. Chem. Solids*, 2020, **136**, 109141.

127 T. Hou, Q. Li, Y. Zhang, W. Zhu, K. Yu, S. Wang, Q. Xu, S. Liang and L. Wang, *Appl. Catal. B Environ.*, 2020, **273**, 119072.

128 J. Qian, S. Zhao, W. Dang, Y. Liao, W. Zhang, H. Wang, L. Lv, L. Luo, H.-Y. Jiang and J. Tang, *Adv. Sustain. Syst.*, 2021, **5**, 2000282.

129 W. Gao, X. Li, S. Luo, Z. Luo, X. Zhang, R. Huang and M. Luo, *J. Colloid Interface Sci.*, 2021, **585**, 20–29.

130 A. A. Khan, M. Tahir and A. Bafaqeer, *Energy \& Fuels*, 2020, **34**, 9810–9828.

131 J. Li, Q. Zhang, Y. Zou, Y. Cao, W. Cui, F. Dong and Y. Zhou, *J. Colloid Interface Sci.*, 2020, **575**, 443–451.

132 H. Jiang, Z. Hu, C. Gan, B. Sun, S. Kong and F. Bian, *Mol. Catal.*, 2021, **504**, 111490.

133 X. Liu and C. Chen, *Mater. Lett.*, 2020, **261**, 127127.

134 K. Wu, S. Song, H. Wu, J. Guo and L. Zhang, *Appl. Catal. A Gen.*, 2020, **608**, 117869.

135 Z. Miao, G. Wang, X. Zhang and X. Dong, *Appl. Surf. Sci.*, 2020, **528**, 146929.

136 X. Wang, Y. Yang, G. Lu, G. Shi, Y. Wang, R. Wang, X. Xie and J. Sun, *Appl. Surf. Sci.*, 2020, **531**, 147101.

137 H. Zhang, M. Li, C. Zhu, Q. Tang, P. Kang and J. Cao, *Ceram. Int.*, 2020, **46**, 81–88.

138 L. Chen, X. Ye, S. Chen, L. Ma, Z. Wang, Q. Wang, N. Hua, X. Xiao, S. Cai and X. Liu, *Ceram. Int.*, 2020, **46**, 25895–25904.

139 Z. Wu, Y. Liang, X. Yuan, D. Zou, J. Fang, L. Jiang, J. zhang, H. Yang and Z. Xiao, *Chem. Eng. J.*, 2020, **394**, 124921.

140 T. Xu, J. Wang, Y. Cong, S. Jiang, Q. Zhang, H. Zhu, Y. Li and X. Li, *Chinese Chem. Lett.*, 2020, **31**, 1022–1025.

141 H. Liu, C. Yang, X. Jin, J. Zhong and J. Li, *Colloids Surfaces A Physicochem. Eng. Asp.*, 2020, **603**, 125239.

142 J. Chen, H. Zheng, Y. Zhao, M. Que, X. Lei, K. Zhang and Y. Luo, *J. Phys. Chem. Solids*, 2020, **145**, 109565.

143 L. Zhang, J. Yang, T. Xie, S. Feng and L. Xu, *Mater. Des.*, 2020, **192**, 108772.

144 Q. Luo, J. Yang, Y. Wu and Q. Cai, *Micro Nano Lett.*, 2020, **15**, 764–768.

145 H. Song, Y. Wang, Z. Ling, D. Zu, Z. Li, Y. Shen and C. Li, *Sci. Total Environ.*, 2020, **746**, 141009.

146 B. Shao, Z. Liu, G. Zeng, Y. Liu, Q. Liang, Q. He, T. Wu, Y. Pan, J. Huang, Z. Peng, S. Luo, C. Liang, X. Liu, S. Tong and J. Liang, *Appl. Catal. B Environ.*, 2021, **286**, 119867.

147 B. Sun, F. Tao, Z. Huang, W. Yan, Y. Zhang, X. Dong, Y. Wu and G. Zhou, *Appl. Surf. Sci.*, 2021, **535**, 147354.

148 N. My Tran, Q. Thanh Hoai Ta and J.-S. Noh, *Appl. Surf. Sci.*, 2021, **538**, 148023.

149 Z. Zhuge, X. Liu, T. Chen, Y. Gong, C. Li, L. Niu, S. Xu, X. Xu, Z. A. Alothman, C. Q. Sun, J. G. Shapter and Y. Yamauchi, *Chem. Eng. J.*, 2020, 127838.

150 M. Yu, H. Liang, R. Zhan, L. Xu and J. Niu, *Chinese Chem. Lett.*, , DOI:10.1016/j.cclet.2020.11.069.

151 X. Meng, J. Song, J. Ren and J. Zhu, *CrystEngComm*, 2021, **23**, 1507–1516.

152 T. Ke, S. Shen, K. Rajavel, K. Yang and D. Lin, *J. Hazard. Mater.*, 2021, **402**, 124066.

153 Z. Yuan, H. Huang, N. Li, D. Chen, Q. Xu, H. Li, J. He and J. Lu, *J. Hazard. Mater.*, 2021, **409**, 125027.

154 S. Vigneshwaran, C. M. Park and S. Meenakshi, *Sep. Purif. Technol.*, 2021, **258**, 118003.

155 H. Wang, L. Chen, Y. Sun, J. Yu, Y. Zhao, X. Zhan and H. Shi, *Sep. Purif. Technol.*, 2021, **265**, 118516.

156 X. Feng, Z. Yu, Y. Sun, M. Shan, R. Long and X. Li, *Sep. Purif. Technol.*, 2021, **266**, 118606.

157 X. Liu, Q. Liu and C. Chen, *Vacuum*, 2021, **183**, 109834.

158 B. Ahmed, A. El Ghazaly and J. Rosen, *Adv. Funct. Mater.*, 2020, **30**, 2000894.

159 X. Zhao, D. E. Holta, Z. Tan, J.-H. Oh, I. J. Echols, M. Anas, H. Cao, J. L. Lutkenhaus, M. Radovic and M. J. Green, *ACS Appl. Nano Mater.*, 2020, **3**, 10578–10585.

160 V. Natu, J. L. Hart, M. Sokol, H. Chiang, M. L. Taheri and M. W. Barsoum, *Angew. Chemie Int. Ed.*, 2019, **58**, 12655–12660.

This journal is © The Royal Society of Chemistry 20xx

Please do not adjust margins